**Study of Semiconductor Heterostructures
with Embedded Quantum Dots:
*Micropillars and Photodetectors***

Carlos Alberto Parra Murillo

June 2009

Study of Semiconductor Heterostructures with Embedded Quantum Dots

Micropillars and Photodetectors

Carlos Alberto Parra Murillo

Adviser
Prof. Dr. Paulo Sérgio Soares Guimarães
Co-Adviser
Dr. Herbert Vinck Posada

Thesis presented to
UNIVERSIDADE FEDERAL DE MINAS GERAIS
in partial fulfillment of the requirements for the title of
MASTER IN PHYSICS
Instituto de Ciências Exatas
Departamento de Física
Belo Horizonte, Brasil

June 2009

A minha senhora Mãe e a minha Irmã.

Na distancia nosso amor

é fortalecido pela esperança.

Amo vocês.

Agradecimentos

- A meus dois grandes amores, minha mãe Maria Pastora e a minha irmã Natalia que na distância sempre me apoiam. É imensa a saudade e maravilhoso o nosso encontro. *Amo vocês...!.*

- Primeiramente quero agradecer ao professor Paulo Sérgio pela sua orientação, a amizade, a paciência, o apoio e confiança, e as múltiplas discussões que permitiram desenvolver esta dissertação.

- Ao Professor Herbert Vinck meu co-orientador, pela confiança que depositou em mim quanto vim trabalhar nesse instituto, seus conselhos e discussões.

- A CAPES e CNPq pela bolsa concedida para a realização desse trabalho.

- Ao pessoal do laboratório de Semicondutores, Alex, Gustavo, Déborah, Andreza, Pablo Thiago e Carlitos Pankiewicz pelo ambiente de trabalho, por terem-me ajudado na aprendizagem desta língua, suas múltiplas correções feitas desde a minha chegada e ao longo da minha estadia aqui no departamento de física.

- A toda a galera da física com quem tive a oportunidade de compartilhar momentos muito agradáveis e memoráveis. Por fazer da minha eterna saudade algo fácil de levar e me fazer sentir mais um deles. Sempre tem um jeito de ser feliz.

- Guilherme Tosi pela amizade e a parceria nessa vida de errante que vou levando nas minhas costas. Leo (Leozim) pelo ânimo constante, os conselhos e as risotadas que dei por conta e culpa dele. Na minha terra costumamos dizer: *'Gênio e figura, até a sepultura'.* Rodriban pela amizade e a paciência.

- A todas essas pessoas que fizeram parte desse processo, das minhas folgas na sala do café, e em outras tantas situações legais. Valeu por tudo!

Contents

List of Figures

Resumo

Neste trabalho estudamos alguns processos ópticos em sistemas semicondutores, em especial, heteroestruturas de dois tipos que contêm pontos quânticos: fotodetectores de infravermelho e pilares de microcavidades. Os pontos quânticos têm a função de fornecer elétrons e/ou quasi-partículas como éxcitons e biéxcitons, fundamentais para a operação de dispositivos baseados em pilares de microcavidades e fotodetectores. A importância dos detectores de infravermelho é enorme, com uma imensa variedade de aplicações, e a relevância das microcavidades têm crescido devido às suas promissoras aplicações tecnológicas. Apresentamos aqui o estudo teórico e experimental destas duas heterostruturas em casos específicos de nosso interesse. Para investigar o acoplamento entre os modos fotônicos e a emissão de pontos quânticos inseridos em pilares de microcavidades, foi implementado um código baseado no software livre CAMFR [*Peter Bienstmann. Cavity modelling framework, http://camfr.sourceforge.net*], que permite-nos modelar dispositivos fotônicos como VCSELs e microcavidades. Mostramos que a partir da análise da intensidade de excitação dos vários modos dos pilares, é possível inferir sobre a polarização dos pontos quânticos neles inseridos. Para auxiliar na interpretação da resposta de fotodetectores de infravermelho baseados em pontos quânticos semicondutores, foi desenvolvido um código na linguagem de programação C, o qual é baseado na diagonalização numérica da equação de Schrödinger na aproximação de massa efetiva, obtendo assim a estrutura de níveis de energia e funções de onda do sistema. As magnitudes de oscilador são calculadas para quantificar quais são as transições

ópticas mais prováveis, e entender alguns fenômenos interessantes que aparecem no estudo dos detectores de infravermelho. Concluimos que o espalhamento Auger é um processo determinante na resposta desses dispositivos.

Abstract

In this work, we study some of the optical processes that take place into semiconductor systems, specially heterostructures of two types with embedded quantum dots: infrared photodetectors and microcavity pillars. Quantum dots are the source of electrons and/or quase-particles such as excitons and bi-excitons, which are fundamental in the operation of devices based on pillar microcavities and photodetectors. The importance of infrared detectors is enormous, with a huge variety of applications, and the relevance of microcavities have increased due to its promising technological applications. We present here a theoretical and experimental study of these two heterostructures in specific cases of our interest. In order to investigate the coupling between the photonic modes and the emission of quantum dots embedded in microcavity pillars we implemented a code using the free software CAMFR [*Peter Bienstmann. Cavity modelling framework, http://camfr.sourceforge.net*], which allows to model photonic devices such as VCSELs and microcavities. From the analysis of the intensity of excitation of the modes in the pillars, we showed that it is possible to infer on polarization of the emission of the embedded quantum dots. Furthermore, to help in the interpretation of the response of quantum dot infrared photodetectors, we developed a code on the C-language which is based in a numerical diagonalization of Schrödinger equation for the effective mass aproximation, in order to obtain the energy levels and wavefunctions of the system. The oscillator strengths are computed to quantify which are the most probable optical transitions, and to understand some interesting phenomena that appear in the

study of infrared photodetectors. We conclude that Auger scattering has a significant role in the response of these devices.

Chapter 1

Preliminars

In this chapter, we present basic physical concepts used in the rest of this text. Concepts that are important to take into account in order to achieve a better understanding of the developments, schemes, approximations and statements that will be done mainly in the two following chapters. We will begin with a brief description of semiconductor heterostructures in a general framework, and follow describing the two special semiconductor structures which will be studied later.

This dissertation is organized as follows. In the first chapter, we present the basic fundamentals that will be implemented along this work. A brief introduction about semiconductor theory is made, and a description of the present situation on microcavities and infrared photodetectors is presented. In the second chapter, we introduce the microcavity pillar, the theoretical modelling, from a classical point of view, of photonic excitation process, its efficiency and relation with a polarization of the quantum dot emission. In the third chapter, it is presented the implementation of the method introduced by Gangopadhyay and Nag [*S. Gangopadhyay e B R Nag. Energy levels in three-dimensional quantum confinement structures, Nanotechnology, vol. 8, 1997*] to study of photodetector structures of our interest. Finally, conclusions and perspectives

are presented, and an appendix with an introduction to the use of the numerical codes is made.

1.1 Semiconductor Heterostructures

Before we describe what a semiconductor heterostructure is, we need to define some concepts from Solid State Physics. This successful branch of physics considers how the large-scale properties of solid materials result from their atomic-scale properties. The number of atoms forming a specific material is of the order of 10^{23}, and its properties are not the same as those of single atoms, as illustred in the figure (1.1), where we see the split of the energy levels when the inter-atomic distance R is reduced (a,b). When N atoms are considered, it is found that there are energy bands (see Fig. 1.1-c) consisting of N levels, one of each single atom, which form a quasi-continuous because the energy difference between neighboring levels is negligible ($\sim 10^{-23}~eV$).
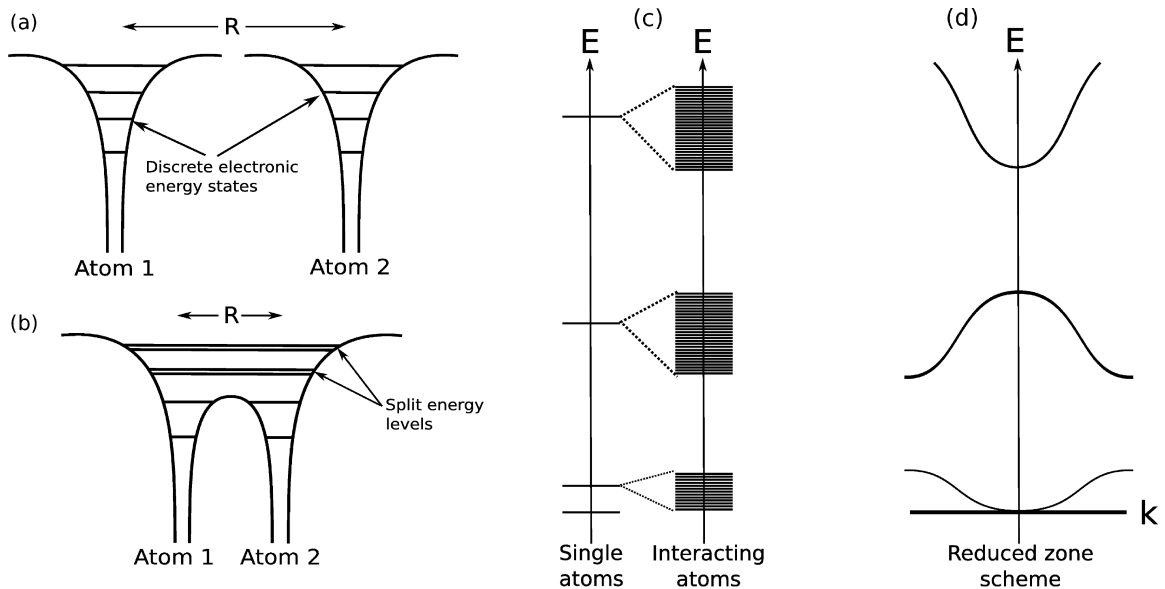
Figure 1.1: Electronic states for two non-interacting atoms (a), and two interacting atoms (b). Band structure and reduced zone scheme for N interacting atoms (c,d).

The band structure, $E = E(k)$, is obtained by considering the N atoms periodically

3

arranged such that the electron wavefunction in the resulting lattice is given by

$$\phi_{\vec{k},i}(\vec{r}) = e^{i\vec{k}\cdot\vec{r}}u_{\vec{k},i}(\vec{r}), \tag{1.1}$$

where $u_{\vec{k},i}(\vec{r}) = u_{\vec{k},i}(\vec{r}+\vec{R})$, for $\vec{R}$ being the lattice vector. The solutions (1.1) are known as electron Bloch-functions that solve the Hamiltonian $\hat{H} = \hat{H}_0 + \hat{U}(\vec{r})$, with $\hat{U}(\vec{r})$ the periodic potential with $\vec{R}$ as period. The Bragg condition allows one to know that just by considering independent wave vectors in the First Brillouin Zone (FBZ-unit cell in the reciprocal space) the rest of the band structure is totally determined. Thus, it is possible to define the so-called reduced zone scheme, in which all $\vec{k}$'s are transformed to lie in the FBZ (see Fig. 1.1-d). This scheme is useful, since when the electrons make a transition from one state to another under the influence of a translationally invariant operator, k is conserved [30, 3, 49, 29], whereas in the extended zone scheme k is conserved only to a multiple of $2\pi/R$, however these two schemes are equivalent.

Having obtained the band structure, we want to fill these bands with electrons taking into account the Fermi-Dirac statistics. Thus, if we assume $T = 0\ K$, there will be energy bands completely filled and partly filled or empty bands. The uppermost completely filled band, that is, the completelly filled band with the highest energy, is called "valence band"(VB), while the partly filled or empty band with lowest energy is called "conduction band"(CB). The energy region close to the top of the valence band and the bottom of the conduction band determines not only the optical properties, but also the magnetic properties and the electronic contributions to the conductivities of electricity and of heat in semiconductor materials. In this way, the band structure determines what kind of material we have. If the band with the highest energy which is occupied by electrons is partly-filled, or if a completely filled band overlaps with an empty or partly-filled band, we have a metal (see Fig. 1.2-(a,b)). If, on the other hand, the filling procedure gives one or more completely-filled bands separated by a gap E_g from the

4

first empty bands, we have a semiconductor (see Fig. 1.2-c) [30] for

$$0 < E_g \lesssim 4 \; eV, \tag{1.2}$$

and an insulator for

$$E_g \gtrsim 4 \; eV. \tag{1.3}$$
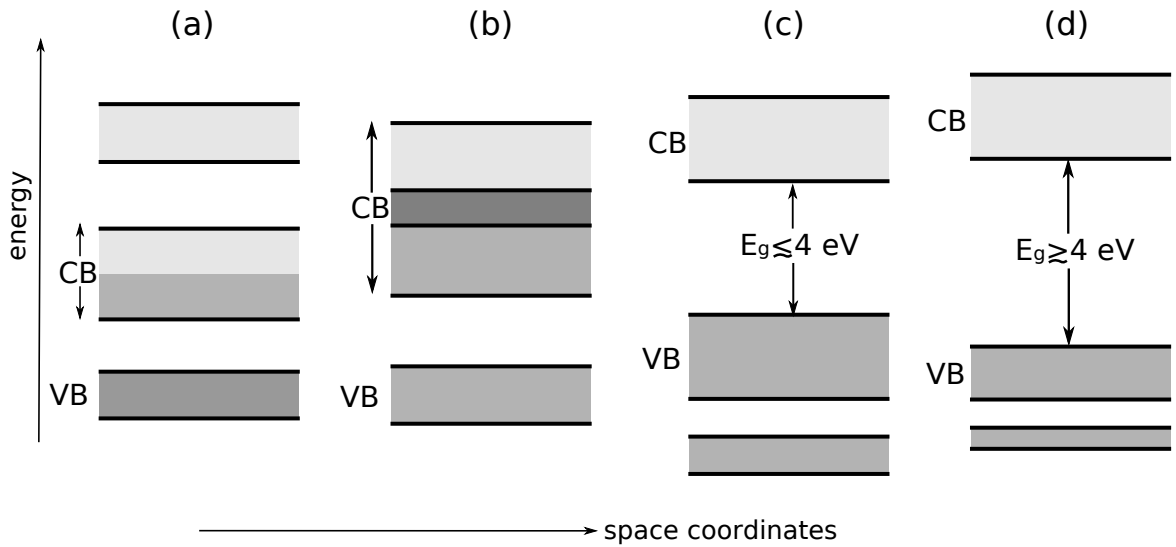
Figure 1.2: Occupation of the bands for a metal (a,b), a semiconductor (c), and an insulator (d).

Depending on size of the gap, the semiconductors are called narrow-gap semiconductors, for $0 < E_g \lesssim 0.5 \; eV$ or wide-gap semiconductors, for $2 < E_g \lesssim 4 \; eV$. In the range $0.5 \lesssim E_g \lesssim 2 \; eV$ we find the usual semiconductors Ge, GaAs and Si. But this is not the only one way to classify them, of course. A very important distinction is between the direct-gap semiconductors, in which the valence band maximum and the conduction band minimum are located at the same value of wavevector k in the band structure, usually $k = 0$, and the indirect-gap semiconductors (see Fig. 1.3), where the minimum of the CB and the maximum of the VB occur at different k values. Optical transitions at the gap energy, i.e., absorption or emission of photons with minimum energy, require

an additional particle such as a phonon in the indirect-gap semiconductors in order to conserve $\vec{k}$.
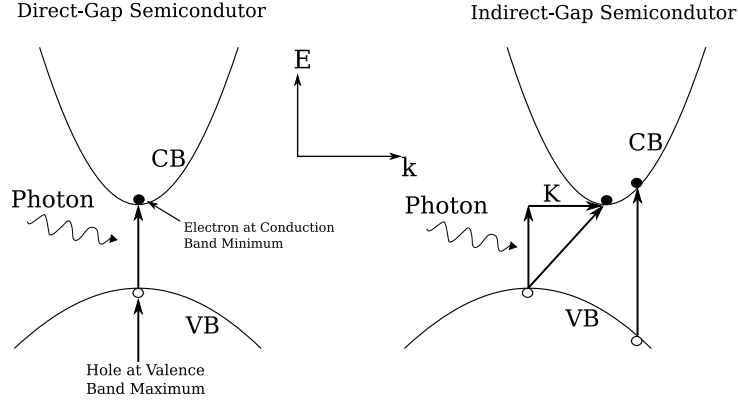
Figure 1.3: Optical excitations in direct and indirect gap semiconductors. Direct transition occurs in direct gap semiconductors, whereas in indirect gap semiconductors an additional wavevector K, involving a phonon, is required for a transition with the minimum energy.

An important effect in excitation processes such as the ones shown in Fig. (1.3) is the creation of a particle so-called "hole"in the valence band, which has the properties of the electron that has been removed from this band, i.e, $q_h = -q_{re}$, $\vec{k}_h = -\vec{k}_{re}$, and spin $\sigma_h = -\sigma_{re}$. Other particle that can be formed in these processes is the so-called "exciton"which consists of a bound electron-hole pair. The exciton is more correctly called a quasi-particle since it is a bound state of two particles. Its life time, or recombination time, is of the order of nanoseconds, and it is usually seen in photoluminescence measurements. We will show later that this particle can be understood as a classical dipole for non-magnetic materials where the spin effects are neglected.

In general, the effect of the internal forces on an electron inside a semiconductor material can be taken into account using the concept of effective mass [29]. Throughout this work, we use the so-called effective mass approximation [30], where the effective mass depends on the dispersion relation as

6

$$\frac{1}{m_{eff}} = \frac{1}{\hbar^2}\frac{\partial^2}{\partial k_i \partial k_j}E(\vec{k}), \tag{1.4}$$

and according to the properties of the band structure, both electron and hole have positive effective mass, even if the curvature of the valence band is negative [30]. The Schrödinger equation in the effective mass approximation is given by

$$-\frac{\hbar^2}{2}\nabla\left(\frac{1}{m^*(\vec{r})}\cdot\nabla\right)\psi(\vec{r}) + V(\vec{r})\psi(\vec{r}) = E\psi(\vec{r}), \tag{1.5}$$

with m^* the effective mass, from which we can obtain the band structure of the material. There are several method to compute the band structure, some of the most used are the so-called $k \cdot p$ method [27] and the tight-binding model [3, 49]. Depending of the complexity of the structure we use the most convenient. Here in this work, we will solve equation (1.5) by direct diagonalization for structures of our interest.
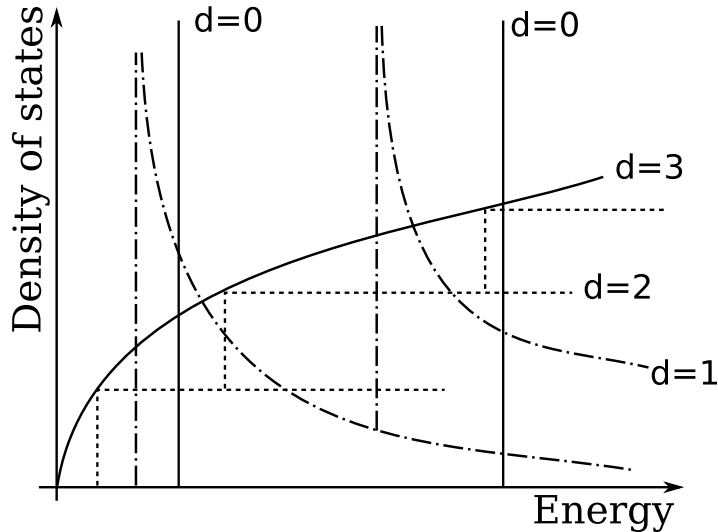
Figure 1.4: Schematic drawing of the density of states as function of energy for three-, and two-, one- and zero-dimensional systems in the effective mass approximation.

Currently, structures with reduced dimensionality in one, two or three directions, are being intensively investigated due to the great variety of their technological applications.

7

The reduction in dimensionality alters the density of states [30], which is given by

$$CB \; : \; D(E) = (E - E_g)^{d/2-1}; \quad E > Eg \qquad (1.6)$$

$$VB \; : \; D(E) = E^{d/2-1}; \quad E > 0; \quad d = dimensionality, \qquad (1.7)$$

as shown in the Figure (1.4). The structures for each dimensionality, i.e., for $d = 3$, $d = 2$, $d = 1$ and $d = 0$, are usually called *Bulk*, *Quantum Wells*, *Quantum Wires* and *Quantum Dots* [30, 49]. Quantum dots are also called quantum boxes, artificial atoms or nano crystals. They have discrete energy levels due to the three-dimensional confinement, and have many important potential applications.

Finally, we define a semiconductor heterostructure as a combination of different semiconductor materials which are grown one on top of another by using epitaxial techniques such as Molecular Beam Epitaxy (MBE) and Chemical Vapor Deposition [49]. The heterostructure performance depends on the properties of the interface between the materials involved, the heterojunction, on the effective mass of the two materials, on their energy gap, strain in the interface, and the band offsets [49, 20, 45, 37, 9]. Three types of heterojunctions, are shown in Figure (1.5).
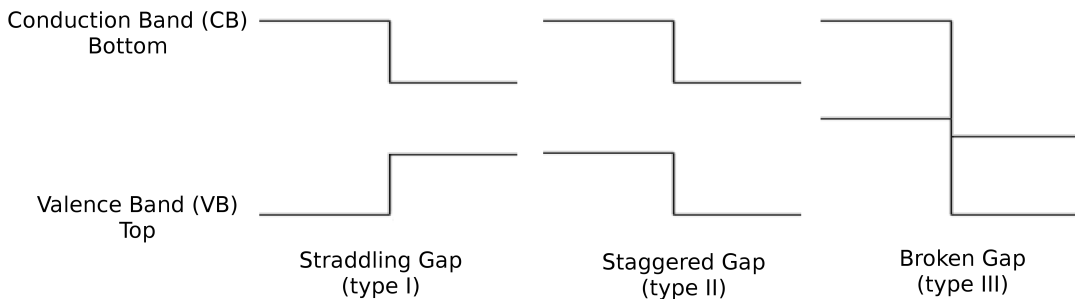
Figure 1.5: The three types of semiconductor heterojunctions organized by band alignment.

8

In our work, all heterojunctions are of type I. The presence of charge, i.e, electrons or holes, in the material leads to the modulation of the CB(VB) profile, which can be computed by solution of the Poisson for the electrostatic potential $\phi(\vec{r})$

$$\nabla^2 \phi(\vec{r}) = -\frac{\rho(\vec{r})}{\epsilon\epsilon_0}. \tag{1.8}$$

where ϵ is the relative dielectric function.

Along this work, we will describe different heterostructures, and all what was exposed above will help us to understand the results and the interesting phenomenology that takes place in these structures. In the next section, we describe two types of devices, microcavities and infra-red photodetectors, which are our structures of interest in this work.

1.2   Optical Microcavities

The optical microcavity is a structure formed by a region sandwiched between reflecting faces that allow the confinement of light (photons) with wavelengths well defined, the so-called modes. These are stationary waves which result from the destructive and constructive interference caused by multiple reflections in the interfaces between the material from which the cavity is made and its surrounding materials. The refractive index contrast between the materials of the cavity, reflecting faces and surrounding, is relevant because it also helps to improve the confinement, which is quantified by the quality factor Q defined as

$$Q = \omega_0 \times \frac{Energy\ storaged\ by\ the\ cavity}{Power\ dissipated\ by\ the\ cavity}, \tag{1.9}$$

or in a simpler and more well known way

$$Q = \frac{\lambda_0}{\Delta\lambda} = \frac{\omega_0}{\Delta\omega}, \tag{1.10}$$

where λ_0 (ω_o) is the mode wavelength (frequency) and $\Delta\lambda$ ($\Delta\omega$) is the Full Width at Half Maximum (FWHM) of the mode spectral lineshape. An important parameter is the modal volume defined as the effective spatial region where the electromagnetic mode exists. It is calculated as follows:

$$V = \frac{\iiint \epsilon(\vec{r})|E(\vec{r})|^2 d^3\vec{r}}{max(\epsilon(\vec{r})|E(\vec{r})|^2)}, \tag{1.11}$$

with $\epsilon(\vec{r})$ the dielectric function. Figure (1.6) shows some types of microcavities with their corresponding quality factors and modal volumes. The first of these devices, the micropillar (a) has attracted much attention recently for applications such as single-photon sources. It offers relative high Q and small modal volume, and the possibility to incorporate quantum dots as emitters. The Bragg mirrors at the top and bottom provide one dimension of cavity confinement, whereas air-dielectric guiding provides the lateral confinement. We will describe and discuss this device in detail in chapter 2. Y. Yamamoto's group from Stanford University was one of the first groups that grew and studied amply the micropillar features [46, 38], and a great quantity of papers have been published in the last years studying this system and its promising applications.

The structures shown in (b,e) have a special set of modes, which live on the cavity surface, and are called whispering gallery modes. However, these modes are not exclusive of this type of microcavities. It has been shown that by lateral excitation of micropillars these modes can form part of the set of modes for these structures [4]. The whispering modes are similarly excited in microspheres, microtoroids and microdisks, by coupling from a fiber-taper waveguide and subsequently guided within and along the periphery of the microcavity. We can see that its quality factors are in general greater than mi-

cropillar quality factors.
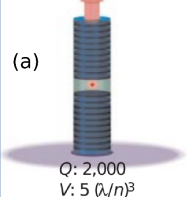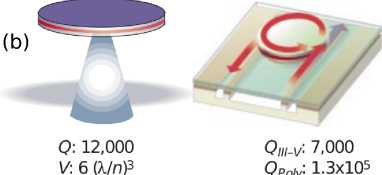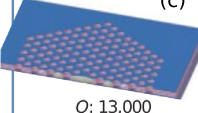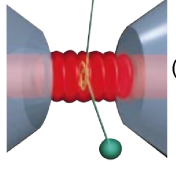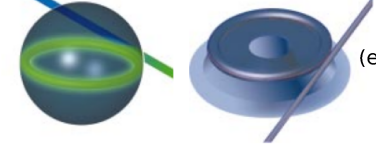
	Fabry–Perot	Whispering gallery		Photonic crystal
High Q	(a) Q: 2,000 V: 5 $(\lambda/n)^3$	(b) Q: 12,000 V: 6 $(\lambda/n)^3$	Q_{III-V}: 7,000 Q_{Poly}: 1.3x10^5	(c) Q: 13,000 V: 1.2 $(\lambda/n)^3$
Ultrahigh Q	(d) F: 4.8×10^5 V: 1,690 μm³	Q: 8×10^9 V: 3,000 μm³	(e) Q: 10^8	

Figure 1.6: Types of microcavities and their confinement features [44].

The atom trap is other type of microcavity, in which the atomic centre of mass motion for ultracold atoms, i.e., atoms with thermal energy smaller than the coupling energy $\hbar\Omega$ in a strongly coupled system, is altered by interaction with the vacuum cavity mode, which is similar to the Fabry-Perot resonator (see Fig. 1.6-d). Ω is the Rabbi coupling frequency. The atom inside the trap (cavity) entrains in an orbital motion before scaping, thus, because the coupling energy depends on the amplitude of the vacuum cavity field near the atom, optical transmission probing of the cavity during the atomic entrainment acts as an ultrasensitive measure of atomic location [23, 21]. The most recently studied microcavities are those embedded into a photonic crystal (see fig. 1.6-c), in which they are treated as the defect in the crystal or they can be part of the well-known unit cell of the crystal [25, 13]. This type of device is a very important research topic nowadays and there are many groups working in its fabrication improvement. The quality factor of photonic crystal cavities, theoretically speaking, has been predicted to be of the order of $10^3 - 10^5$ [2]. As in micropillars, in photonic crystals microcavities the growth of quantum dots inside the cavity is easily accomplished. The location and orientation of emission of the quantum dots are fundamental parameters

that determine the efficiency of modal excitation in the cavity [17], for this reason, the growth of quantum dots precisely located has been studied, in order to create structures of high performance [36].

Even though Q and V are the most relevant microcavities parameters, there are alternative measures of performance for these structures, for example, the **cavity finesse** [44, 10, 16], which does not include the propagation effects as does the Q factor.

All these microcavities properties exposed above make these systems excellent candidates to recent and future applications in optical telecomunications, quantum optics, and diverse areas that involve optical devices.

1.3 Infrared Photodetectors

The mid-infrared photodetectors are another kind of semiconductor structure usually based in semiconductors made of elements III and V of the periodic table. The research and development in this area comes from the need to fabricate opto-electronics devices that have many applications in, e.g, telecommunications, aerospace and defense. The particular application determines the infrared region for which we need to design the device. In general, only a specific region of the spectrum is of interest and sensors are designed to collect radiation only within a specific bandwidth, although broadband detectors are also of some interest. The infrared region is subdivided in various regions:

- Near-Infrared (wavelength from ~ 0.5 μm to ~ 1.4 μm): used for fiber optic telecommunication and night vision.

- Short-Wavelength Infrared (λ from ~ 1.4 μm to ~ 3 μm): in this region the water absorption increases significantly, but it is also good for long-distance telecommunications.

- Mid-Infrared (λ from $\sim 3\ \mu m$ to $\sim 8\ \mu m$): interesting region for defense applications, as guided missile technology of $3-5\ \mu m$.

- Long-Wavelength Infrared (λ from $\sim 8\ \mu m$ to $\sim 15\ \mu m$): this is the "thermal imaging"region, in which sensors can obtain a completely passive picture of the outside world based on thermal emissions only and requiring no external light or thermal source such as the sun, moon or infrared illuminator. Sometimes is called far-infrared region.

Presently, the state-of-the-art detectors are quantum well infrared photodetectors (QWIP) [32], indium antimonide (InSb) detectors, and mercury-cadmium-telluride detectors (HgCdTe), however several different authors have proposed a new kind of detectors, the quantum dot infrared photodetectors (QDIP), which have some advantages over the infrared radiation detectors mentioned above. We can say the QDIPs are part of the third-generation of infrared detectors [41]. The QDIP is similar to the QWIP, in the sense that both are based in the intersubband level transition in either conduction band or the valence band in the heterostructure designed to work in a specific wavelength. The main differences between these devices are, first the QDIP allows normal incidence, this is, the incident light normal to the wafer along the growth direction is expected to cause transitions, which greatly simplifies the fabrication process. Second, a significant reduction of the dark current is obtained, which makes it possible to operate the detector at temperatures higher than a QWIP. Recently, tunneling structures that combine quantum dots with quantum wells and with potential barriers have been proposed in order to obtain more selective detectors and also to reduce the dark current [41]. This kind of multilayered structures promises the future development of infrared photodetectors that operate at moderately low temperatures or even at room temperature. Examples of applications of infrared detectors are shown in Figure (1.7).
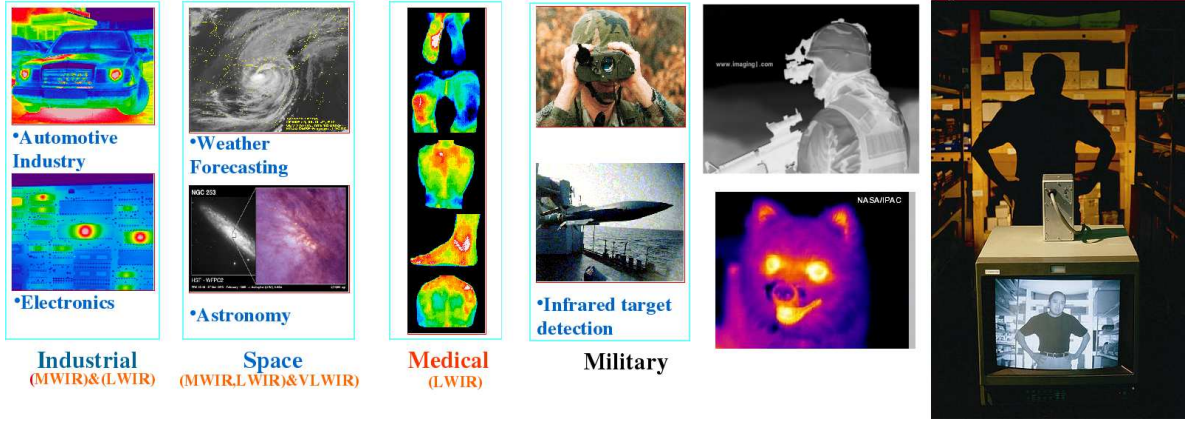
Figure 1.7: Infrared images and applications.

So far, we made a brief review of infrared photodetectors, now we define the main physical features that need to be studied and optimized, in order to understand the performance of these devices. We begin with the dark current, which can be estimated by counting the mobile charge density thermally excited and multiplying by the carrier velocity as follows

$$\langle j_{dark} \rangle = e v n_{3D}, \tag{1.12}$$

where v is the drift velocity and n_{3D} the density of thermally excited carriers, which is given by

$$n_{3D} = 2 \left(\frac{m_b k_B T}{2 \pi \hbar^2} \right)^{3/2} exp \left(-\frac{E_a}{K_B T} \right), \tag{1.13}$$

where m_b is the effective mass of the region where the dark current is calculated, and E_a is the thermal activation energy, which is equal to the difference between the Fermi energy and the first continuum level in the structure. This current is the major cause of noise in the detection and depends strongly on the temperature, becoming $2 \ A/cm^2$ for temperatures near $300 \ K$ [5]. Obviously, that is an effect that needs to be reduced, and that is possible by use of a QDIP structure combined with potential wells and barriers, in order to create a filter, as mentioned before. The photocurrent j_{photo} is defined as

14

follows

$$\langle j_{photo} \rangle = e\sigma I \langle n \rangle, \tag{1.14}$$

where σ is the cross section of the electron excitation, I is the radiation intensity and n the density of electrons optically excited. In this way, we can define the so-called responsivity R of the device as

$$R = \frac{\Delta j}{e\hbar\omega I} = \frac{e}{h\nu}\eta g, \tag{1.15}$$

with $\Delta j = j_{photo} - j_{dark}$, η defined as the absorption efficiency and g the photoconductive gain

$$g = \frac{\tau_{life}}{\tau_{trans}}, \tag{1.16}$$

where τ_{trans} is the transit time across the device, and τ_{life} is the lifetime of the photoexcited electron. The figure of merit used to evaluate the performance of most QWIPs and QDIPs is the specific detectivity ($D*$), which is a measure of signal-to-noise ratio and it is given by

$$D^* = \frac{R\sqrt{Af}}{\sqrt{4\langle j_{dark} \rangle g_{device}\Delta f}}, \tag{1.17}$$

here, A is the device area, f is the measurement frequency, Δf ($= 1\ Hz$) is the bandwith frequency, g_{device} is the photoconductive gain of the device, which, in the case of a $QDIP$, is given by

$$g = \frac{(1 - P_c)}{(MFP_c)}, \tag{1.18}$$

where P_c is the capture probability, and F is the fill factor [34]. The features mentioned before have been studied theoretically and experimentally [34, 5, 41], and the number

of papers in this topic continues to increase.

Chapter 2

Pillar Microcavities with Embedded Quantum Dots

In this chapter, we present a detailed explanation about the exciton-photonic modes interaction in *pillar microcavities* in order to understand how this can be made more efficient and also to explain the surprising experimental results obtained and the interesting consequences of these results. We begin by introducing the characteristics of the system and the modelling made. The work reported here was published in the article: **Optics Express Vol. 16, No 23, pag.19201, (2008)**.

2.1 Micropillar (DBR Micropost)

The pillar microcavity is usually fabricated from a semiconductor heterostructure grown by Molecular Beam Epitaxy (MBE) which consists in a λ-thick GaAs microcavity with lower and upper Bragg mirrors composed of, respectively, N_1 and N_2 periods, each one consisting of $(\lambda/4)$-thick GaAs and $Al_xGa_{1-x}As$ layers with refractive indexes n_{GaAs} and n_{AlGaAs}. Here λ must be understood as the wavelength of radiation in the material. In the middle of a cavity a InAs layer is grown to create self-assembled quantum dots by the Stranski-Kastranov method. These quantum dots are the sources of excitons that

are fundamental for this kind of studies. It is known that the geometry of the pillar determines what kind of photonic modes can be supported by the cavity, for instance, if the cavity is planar, the family of modes is $\{TE, TM\}$ and there is no mixture between them as in the case of circular and elliptical pillars; in our work the micropillars studied have cylindrical geometry and were fabricated by Electron Beam Lithography (EBL) and Inductively Coupled Plasma Reactive Ion Etching (ICPRIE) (see Fig. 2.1) [12].
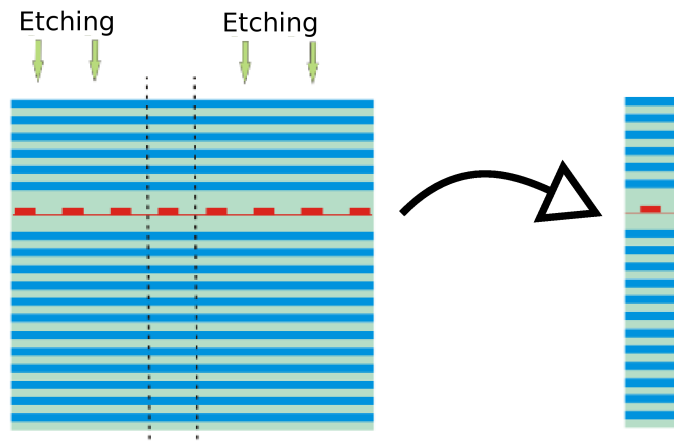
Figure 2.1: Fabrication of a micropillar with embedded quantum dots using EBL and ICPRIE.
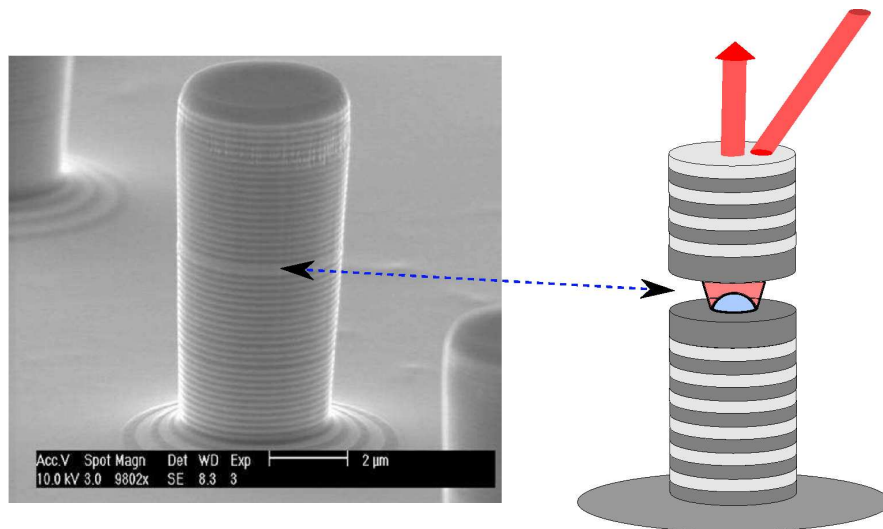
Figure 2.2: (*Left*) Cylindrical micropillar. Image taken by Scanning Electronic Microscopy. (*Right*) Schematic process of excitation of excitons by mean of external source.

As result of this process we have the pillar shown in the Scanning Eletronic Microscopy technique image of Figure (2.2). But, why is it important to design this system with all these specific characteristics? The first interesting property of this system is the confinement of photons in the microcavity due to two relevant processes: (a) contrast between refractive indexes, in our case 3.510 to 2.497 for the cavity and the materials up and down this respectively. Laterally there is air, so the contrast is large, 3.510 to 1.0. These contrasts allow that by total internal reflection (TIR) a wave can propagate along a particular direction as in the case of a waveguide. (b) The second important process is the multiple reflections in the interfaces between the materials in the Bragg mirrors which, by constructive and destructive interference, stationary waves, also called *modes*, are created in the cavity. The lifetime of the cavity modes can be increased by increasing the number of the Bragg reflectors, because these damp the outgoing radiation thus increasing the confinement due to its high reflectivity, and therefore making light storage possible. The most interesting phenomenon that is observed in this system is the so-called Purcell effect [40] which establishes that the radiation properties of an atom can be modified controlling the boundary conditions of the electromagnetic field with mirrors or cavities. The existence of this effect means that it is possible to enhance the spontaneous emission rate, also called incoherent radiation, and store just coherent radiation in the cavity. In other words, let Γ_0 and Γ be the spontaneous emission rate of an atom that is located inside and outside of the cavity, respectively. The Purcell factor (F) is defined as the ratio between these two emission at the resonance wavelength λ rates. It is possible to show [46] that for any atom-field coupling regime it is given by

$$F = \frac{\Gamma}{\Gamma_o} \sim \frac{3Q\lambda^3}{4\pi^2 V}, \tag{2.1}$$

where Q is the quality factor of the cavity, λ is the frequency of the mode and V is the modal volume as defined in chapter 1 (1.9 and 1.10).

Let us note here that F depends on the ratio Q/V, which must be optimized by increasing Q and decreasing the modal volume V, but these parameters in general vary in opposite ways. For example, a decrease in the pillar size, in order to obtain a small V, will lead to lower Q, due to problems of fabrication and surface losses. Therefore, a compromise between these parameters has to be found. For the strong atom-field coupling phenomenon the parameter to maximize is $Q/\sqrt{V}$ [28, 47].

These interesting properties make the micropillar system a good option for multiple technological applications [44]. For example, a micropillar with embedded quantum dots is a very good single-photon source. This system is equally interesting for fundamental physics studies because some basic principles and phenomena such as quantum interference can be investigated using these devices as sources in, for instance, a Hanbury-Brown-Twiss setup, a Mach-Zehnder interferometer and others.

2.2 Theoretical Modelling

So far, we presented the physical characteristics of our system and how to improve these in order to get the best performance of the devices. Now we show the theoretical model which we implemented to describe the interesting experimental results of microphotoluminescence measurements of an array of nominally identical GaAs/AlGaAs pillars with embedded quantum dots.

2.2.1 Quantum Dot in a Pillar

Let us consider a quantum dot modelled as a permanent electric dipole $\vec{p} = q\vec{d}$, which has six degrees of freedom that determine its position and orientation (polarisation). As a result of the growth process the dot z-position is fixed in the middle of the cavity, and so this coordinate is unchanged. The quantum dot position is controlled by

use of the r and ϕ coordinates. For the dot orientation (polarisation), we need three coordinates, which will be the cylindrical coordinates (r', ϕ', z'). In the figure (2.3) we show a quantum dot with lens shape [14], and its schematic dipole, that we will use to represent its photon emission. The growth directon is along the [001] crystalline axis of the host material.

[001]

[110]

[1$\bar{1}$0]
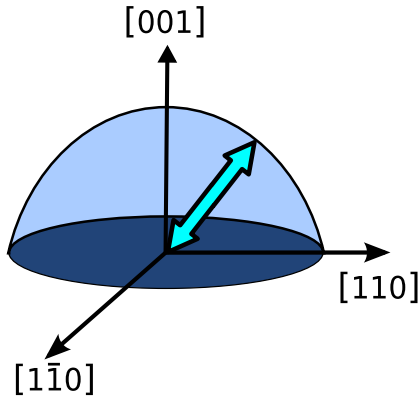
Figure 2.3: A lens-shaped quantum dot shown with the crystalline axes of the host material. The double arrow symbolizes the electric dipole that is used in our model to represent the emission.

Both the position and orientation of emission of the quantum dot are not controllable parameters in the growth process. It has been shown experimentally and theoretically that when an exciton is created in an InAs/GaAs quantum dot, spatial separation of the electron and the hole may create an oriented dipole. However, this result is not clear since some autors [14] have obtained results which indicate that the electrons are at the bottom of the dot and the holes are located above them, which is exactly the opposite of what band theory predicts [20, 39]. Currently there is not a definitive solution for this controversy, which is probably due to the fact that the dot shape is very relevant. If the dots have azimuthal symmetry around the [001] growth axis, the fundamental excitonic transition is unpolarized as observed in most experimental studies. However, the InAs/GaAs quantum dot is in general asymmetric in shape and composition and is subjected to strain. Therefore, it is not unusual to see polarised emission from such

quantum dots: emission orthogonally polarised along the [1$\bar{1}$0] and [110] crystalline directions have been reported by several authors [15, 31]. Polarization along the [001] growth direction is also seen, although more rarely and mostly for special situations [24, 43]. In this work we present results which show how relevant both position and orientation of the quantum dots are in order to understand some differences in the photoluminescence spectra obtained.

2.2.2   Cavity modes

Principles of classical electromagnetism can be used to study micropillars and similar kinds of photonic systems due to size scale of the structures. The Finite Difference-Time Domain (FDTD) method is one of the techniques frequently used because of the reliability of the results. Some softwares use optimized algoritms allowing their implementation to study complex structure. Among these we mention **MPB** [26], **FullWave** [1] and **CAMFR** [8]. The last one is the tool used by us in this work. In the following we present briefly the physical basis of this software and how we modelated the physical system and the cavity modes.

To understand how **CAMFR** works, first we describe the method so-called *eigenmodes expansion* [6], which works in the following way:

(i) We begin with Maxwell equations with no sources, which are

$$\nabla \cdot \vec{D} = 0 \qquad\qquad (2.2a)$$

$$\nabla \cdot \vec{B} = 0 \qquad\qquad (2.2b)$$

$$\nabla \times \vec{E} = -\frac{\partial \vec{B}}{\partial t} \qquad\qquad (2.2c)$$

$$\nabla \cdot \vec{H} = \frac{\partial \vec{D}}{\partial t} \qquad\qquad (2.2d)$$

These equations can be decoupled using the vectorial identity $\nabla \times (\nabla \times \vec{A}) = (\nabla \cdot \vec{A})\nabla - \nabla^2 \vec{A}$. Combining the Ampére law and the Faraday induction law we obtain the wave equations for each field

$$\frac{1}{\mu\epsilon(\vec{r})}\nabla^2\vec{E}(\vec{r}) = \left(\frac{\omega}{c}\right)^2\vec{E}(\vec{r}) \tag{2.3}$$

$$\nabla \times \left(\nabla \times \frac{1}{\mu\epsilon(\vec{r})}\vec{H}(\vec{r})\right) = \left(\frac{\omega}{c}\right)^2\vec{H}(\vec{r}) \tag{2.4}$$

for which harmonic solutions are normally proposed, as follows

$$\begin{bmatrix} \vec{E}(\vec{r},t) \\ \vec{B}(\vec{r},t) \end{bmatrix} = e^{-i\omega t}\begin{bmatrix} \vec{E}(\vec{r}) \\ \vec{B}(\vec{r}) \end{bmatrix}. \tag{2.5}$$

(ii) Consider a structure that consists of different materials with refractive indexes n_i's. This structure is divided in regions where the refractive index is constant, and the spatial part of the solutions of (2.5) are found for each region, forming a set of eigenmodes $\{E_k, H_k\}$, in which the general solution is expanded as follows,

$$\vec{E}(\vec{r}) = \sum_k A_k E_k(\vec{r})$$

$$\vec{H}(\vec{r}) = \sum_k A_k H_k(\vec{r}).$$

(iii) With each solution totally established, it is necesary to find the fields for the structure by coupling the adjacent regions. For this, there are two schemes:

T-Scheme: The properties of reflection and transmission are computed by use of the matrix transference method, using the boundary conditions for the

electromagnetic fields in the interfaces between each two materials [48]. With this method, that does not depend on the sources, it is possible to calculate either the reflection or transmission spectra. From them is possible to get the energy modes and calculate their quality factor.

S-Scheme: In this, the outward-propagating fields of the structure (non-guided or leaky modes) are related with the inward-propagating fields (guided modes), which allows to study the dissipation in the system by means of the quality factor Q.

The process is applicable for any structure, and the calculation times depend on the geometry. CAMFR has an additional feature, the Perfect Matched Layer method (PML) [7]. This method allows to absorb the unbounded modes at the simulation window boundary in order to eliminate the parasitic reflections.

In the present case, we use cylindrical coordinates for which the transformation equations are given by

$$x = r\,cos\theta$$

$$y = r\,sin\theta$$

$$z = z$$

The wave equations for the z-components of the fields are as follows

$$\left[\frac{\partial^2}{\partial\rho^2} + \frac{1}{\rho}\frac{\partial}{\partial\rho} + \frac{1}{\rho^2}\frac{\partial^2}{\partial\theta^2} + \frac{\partial^2}{\partial z^2} + k^2 - \beta^2\right]\begin{bmatrix} E_z(\vec{r}) \\ B_z(\vec{r}) \end{bmatrix} = 0. \tag{2.6}$$

with general solution

$$\left(AJ_l(k_t\rho) + BN_l(k_t\rho)\right)\left(Ccos(\beta z) + Dsin(\beta z)\right)e^{il\phi}, \qquad (2.7)$$

where $k_t = \sqrt{k^2 - \beta^2}$, with β being the effective vector along the propagation direction z. The other components can be obtained from these, because, by manipulation of the equations (2.2) it is easy to write them in terms of E_z and H_z. For the set of solutions (eigenmodes) to be complete it is necessary to determine the constants, A, B, C and D, which is done by use of the boundary and orthonormalization conditions. The fields are labeled using the conventional notation for waveguide modes, i.e., there are two families of solutions, HE and EH, the so-called hybrid modes. They are defined depending on the ratio E_z/H_z, in this way, if this ratio is greater than 1, we have EH modes and if the ratio less than 1, the modes are HE. In these families, there are two particular sets of *pure* modes. The first of these occurs when the ratio E_z/H_z tends to zero, this means that just H_z is projected along the z direction. These modes are called tranverse electric (TE). The other situation is when the ratio E_z/H_z tends to infinity, so the component projected onto z is E_z and the modes called tranverse magnetic (TM).

Inward and outward-modes of the structure are found expanding in this basis and will be totally determined by use of either the T-Scheme or S-scheme, and so other optical properties can be computed with the CAMFR code. In the next sections, we bring everything together and focus our attention in the study of a quantum dot-dipole interacting with the photonic modes in a micropillar.

2.2.3   Excitonic-Photonic mode interation in the micropillar

The interaction between quantum dot-dipole and a cavity mode from a classical point of view is known to be

$$U_{int} = -\vec{p} \cdot \vec{E}_{lmn}(\vec{r}), \tag{2.8}$$

from which some important details become apparent:

(a) The coupling is maximized for $\vec{E}_{lmn}$ parallel to $\vec{p}$, which could be controlled by changing the dot orientation, but this is at the least difficult to do in practice. In addition, the field lines are not uniformly distributed and therefore the ideal orientation depends on the spatial location of the dot.

(b) The spatial distribution of the field in the cavity also affects this interaction, because the field has variable magnitude in this and it is zero in some regions [33], due to the pattern of stationary waves created. So, the position of the dot is also an important parameter and could be changed in order to optimize the coupling.

(c) It is clear then that the location of the dot and the polarization of its emission are very important in order to obtain a strong coupling with the electromagnetic modes. The development of techniques to grow quantum dots in specific positions, for example, where the field is maximum in order to improve the coupling, has been a lively investigation topic.

The great difficulty from the experimental point of view is that parameters such as dot shape, dot charge distribution and, therefore dipole orientation and position of the dot are random in the fabrication process. In this way, there is no certainty which one of the dots is better coupled with the field, and which are its characteristics. Recently, some [36] works showed progresses in the fabrication of heterostructures with quantum dots highly located in pre-determinated positions.

2.3 Experimental setup

The samples studied in this work were grown by MBE in the Sheffield University, UK, and the experimental measurements were made by **Dr Andreza G. Silva** and **PhD student Pablo T. Valentim** from Universidade Federal de Minas Gerais, Brasil. The density of InAs-dots in the cavity is of the order of 10^{10} cm^{-2} and it was estimated that a number between 20 and 100 dots were randomly located in the central cavity plane. The distributed Bragg reflectors consist of $N_{lower} = 27$ and $N_{upper} = 20$ pairs of GaAs and $Al_{0.8}Ga_{0.2}As$, each one with thickness 69.3 nm and 78.0 nm respectively.
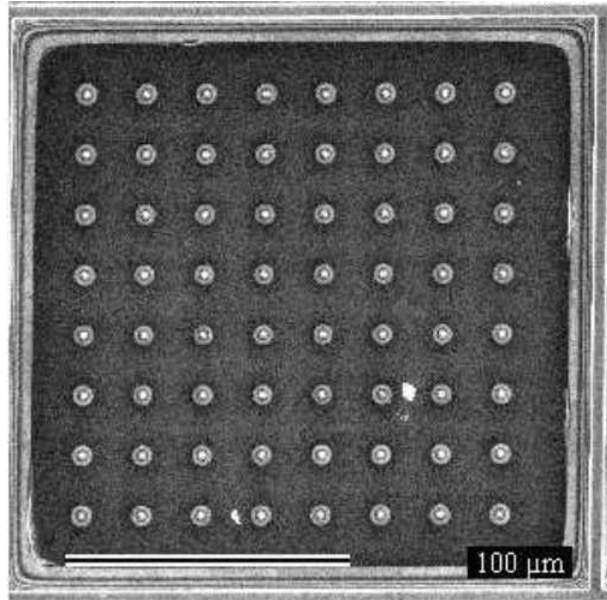
Figure 2.4: Microphotography of the part of the sample studied, from above, showing the matrix of micropillars used in the microphotoluminescence experiment.

In Figure (2.4) it is possible to see the 8×8 matrix of micropillars, from which were chosen 33 nominally identical pillars with circular cross sections of 1.5 μm of diameter. This selection was made choosing those pillars on which neither its fundamental nor the three first excited modes showed a splitting, which would be an indicative of deviations from circular symmetry. The fundamental mode shows a *full width at half maximum* of (0.22 ± 0.005) nm, which corresponds to a quality factor $Q = 4300$, and just the pillars
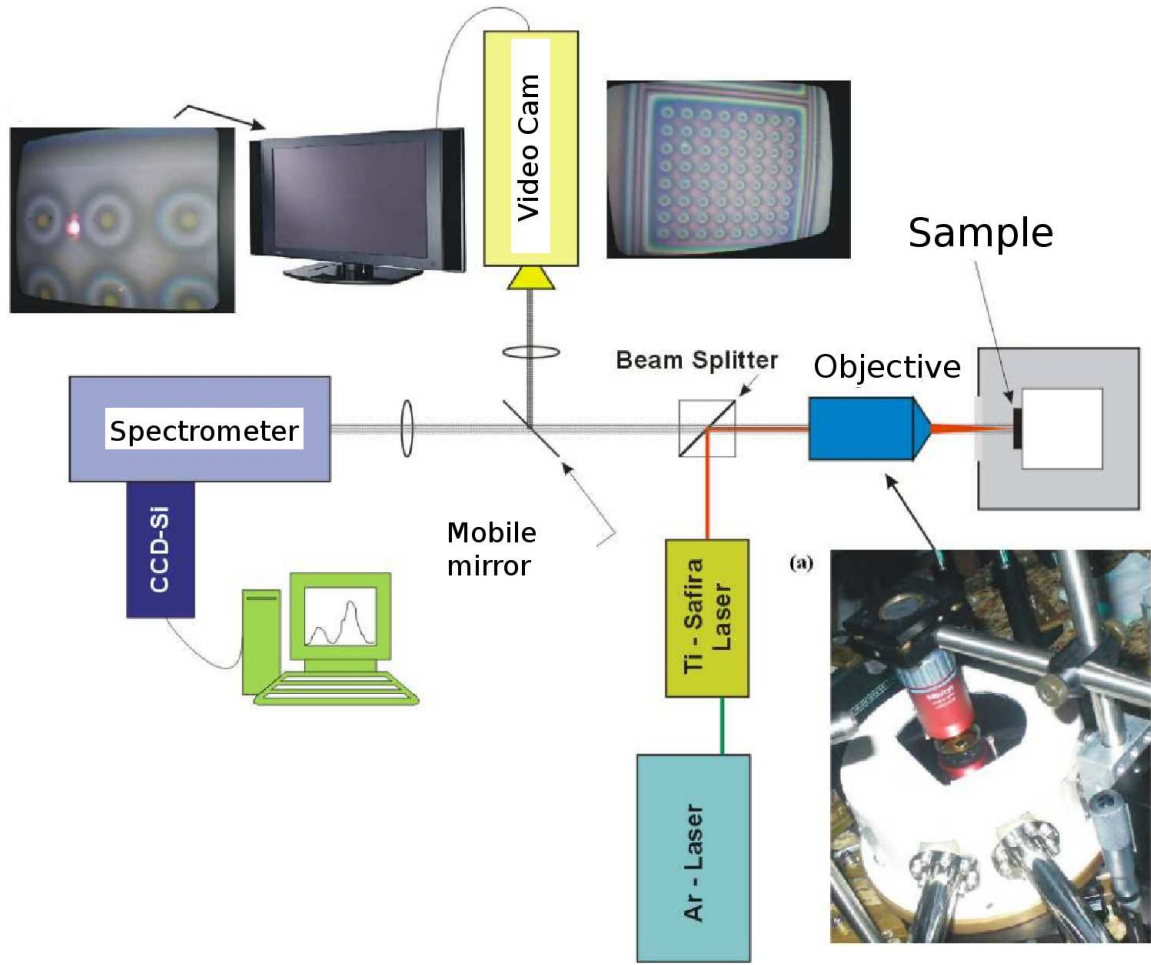
Figure 2.5: Microphotoluminescence experimental setup.

with wavelength in this range are selected. In Figure (2.5) we present the microphoto-luminescence setup used, where the excitation is provided by a titanium-sapphire laser tuned at 740 nm. A microscope objective with numerical aperture of 0.4 is used to focus the excitation beam to a spot with diameter $\leq 2\ \mu m$.

The emission from the micropillar was collected by the same objective, focused on a 0.75 m monocrhomator, and detected by a nitrogen cooled charge-coupled device detector. All these measurements were made with a resolution of 0.05 nm and at $T = 4\ K$ within a helium flow cryostat.

2.4 Results

In order to complement the theoretical modelling, we explain here the principal commands used to compute the desired spectrum of the system. CAMFR code is based in the Python interpreter, which contains a variety of libraries that can be called by a simple python *script*. For example, before the pillar and its characteristics are defined, the libraries need to be imported as follows

```
from camfr import *
```

The comments in the code start with #. By means of the following sequence it is possible to design the structure, First we use the routine `Stack` to define both top and bottom of the pillar. Its argument consists of the half to the cavity plus the `N` Bragg reflectors, as follows

```
# Defining pillar top
top = Stack(2*capa_GaAs(d_GaAs)+N_capas_der*(capa_AlGaAs(d_AlGaAs)+
capa_GaAs(d_GaAs))+space(0))
# Defining pillar bottom
bottom = Stack(2*capa_GaAs(d_GaAs)+N_capas_izq*(capa_AlGaAs(d_AlGaAs)+
capa_GaAs(d_GaAs))+space(0))
# Cavity
cavity = Cavity(top,bottom)
```

where the routine `Cavity` connects these two parts. Each layer is defined using the routine `Circ` (`Slab` in rectangular coordinates) in the following way

```
capa_GaAs = Circ(GaAs_n(r_core)+air_n(work_space-r_core))
```

```
capa_AlGaAs = Circ(AlGaAs_n(r_core)+air_n(work_space−r_core))
```

with `r_core` the pillar radius. Therefore, so we have a layer that consists of two concentric circular cylinders, with the inner one being the circular pillar layer. The space between the cylinders, which has a width `work_space−r_core`, contains air. Here, `work_space` is the lateral size of the simulation window. As we said before (see Sec. 2.2.2), the radiation that reaches the boundary of the simulation window is absorbed for this by use of PML condition. That boundary is located in the wall of the outer cilynder. The dipole parameters are also simple to introduce by the routine `Cavity.set_source`, as follows

```
cavidad.set_source(source_pos,source_orientacion)
```

and both position and orientation of the dipole are controlled by the routine `Coord`

```
source_pos = Coord(r, φ, z)
souuce_orientacion = Coord(r′, φ′, z′)
```

We must take into account that the dipole orientation does not match in all cases with the polarization of the dot emission. For instance, if we have a dipole $(1, 0, 0)$-oriented, this orientation is equivalent to a dot emission [110]-polarized, but if the dipole is $(0, 1, 0)$-oriented, we can not infer the polarization of the dot emission, i.e., it is unpolarized. However, it is possible to write the polarization states of the dot emission in terms of the pure dipole orientations here defined.

With the structure defined, we compute the power flux along the z-direction between `r0=0` and `r1=r_core` by means of the Poynting vector, as follows

```
power_flux = top.ext_S_flux(r0,r1,relative_error)
```

which allows us to compute the photoluminescence spectra (λ,`power_flux`) and study
the variations that these suffer as the pillar and dot parameters are changed. For in-
stance, it is possible to get a good fit of the experimental spectra modifying the refractive
indexes of the materials involved respectively. The refractive indexes values for GaAs
and $Al_{0.3}Ga_{0.7}As$ are 3.5 and 3.0, respectively. However, the actual values depend on
the physical conditions of the experiment such as temperature, which, by creation of
phonons in the crystalline lattice modify the dielectric function of the material, and
therefore the refractive index. The following approximation is reported in the literature
to compute the dependence of the refractive index on the temperature:

$$n(T) = n_0 - 10^{-5}(T - T_0)$$

.

The refractive index also depends on the wavelength and on the Al concentration for
$Al_xGa_{1-x}As$ and it is difficult to determine a priori the exact value of the refractive in-
dexes that should be used. We use the values reported in the literature and do the fine
adjustment by fitting the fundamental mode position of a set of experimental spectra
of micropillars of different diameters, such as the spectra shown in Figure (2.6).

We obtain a good fit of the energy of the peaks in experimental spectra such as those
of the figure (2.6). We also note that the shifts in the energies of the peaks with pillar
diameter are in good agreement with the tendence reported by Gerard et al. [19], where,
for the case of the fundamental mode HE_{11}, its energy decreases up to a saturation
value as the pillar diameter increases. Similar behavior is observed for the quality fac-
tor Q, which increases up to a saturation value, which is the Q value of the planar

31
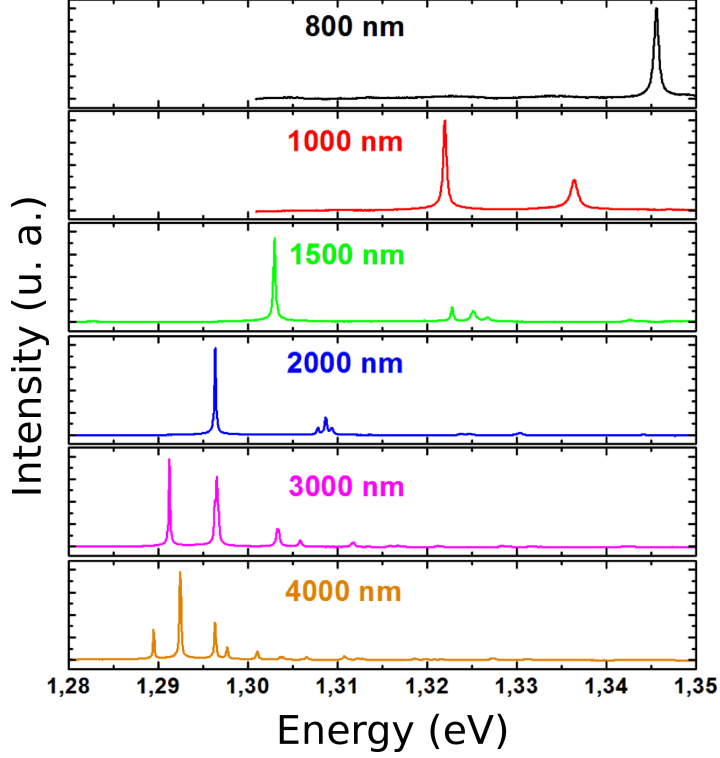
Figure 2.6: Photoluminescence spectra for pillar with different diameters.

microcavity, i.e., the Q value of the microcavity sample as grown, before fabrication ot the pillars. Another important observation here, is that as the diameter of the pillar is increased, the energy separation between the first three excited photonic modes decreases, and they tend to be near the fundamental mode energy. Before showing the results of this study, we present some interesting situations that help us to understand the optical properties of our system.

Figure (2.7) shows the theoretical spectra obtained for different dot parameters. We see that some photonic modes are not excited for some dot orientations and positions, for example, the TE mode is the only one excited for a dot $(0, 1, 0)$-oriented but its intensity is reduced as the dot is near to the center of the cavity. For these low energy spectra, the fundamental mode is the one mostly excited, but we see that its intensity is the smallest for a dot located near the radial boundary. The effect of the radial position
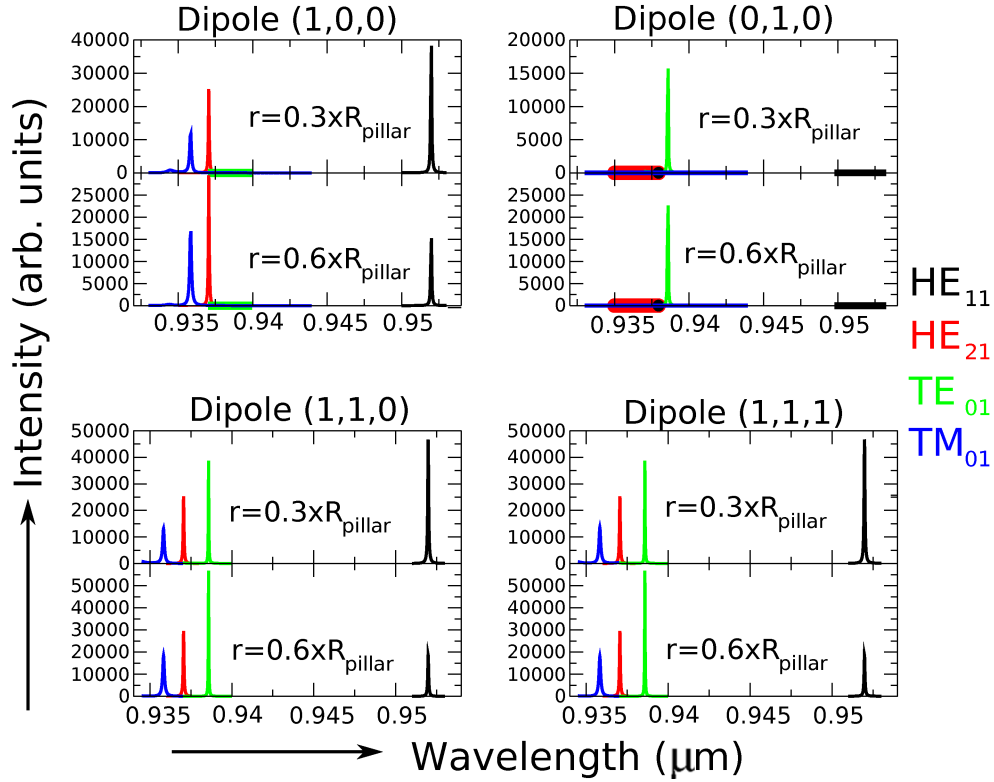
Figure 2.7: Quantum dot position and orientation effect over modal excitation. Dipoles with orientations $(1, 0, 0)$, $(0, 1, 0)$, $(1, 1, 0)$ and $(1, 1, 1)$, located in $r = 0.3R_{Pillar}$ and $r = 0.6R_{Pillar}$, where R_{pillar} is the radius of the pillar.

of the dot in the intensity of the fundamental mode is shown in the figure (2.8) for angular position $\phi = 0$.

A different behavior is seen in Figure (2.9), where we note that the TM mode is the only one excited for a dot $(0, 0, 1)$-oriented, and that its peak intensity varies as the radial dot position changes. The intensity of excitation is relatively small compared with the high excitation intensity of the modes for a dot $(1, 1, 0)$-oriented, as seen in the spectra of Figure (2.10), in which it can be noted that the relative intensity of the three first excited modes is approximaterly constant as the dot radial position changes. For $r = 0$ these modes are not excited.

It is interesting to see how the intensity of the three first excited modes, i.e., the three
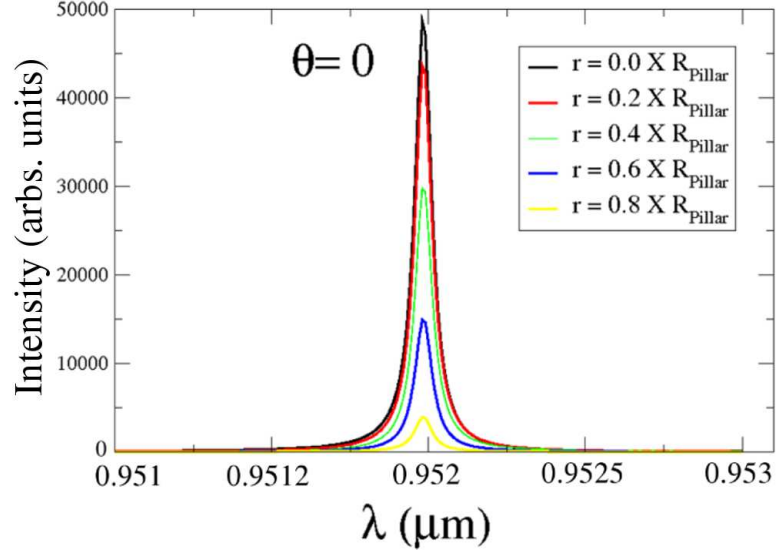
Figure 2.8: Dependence of the intensity of the fundamental mode emission peak with the radial position of a dot $(1, 0, 0)$ oriented.
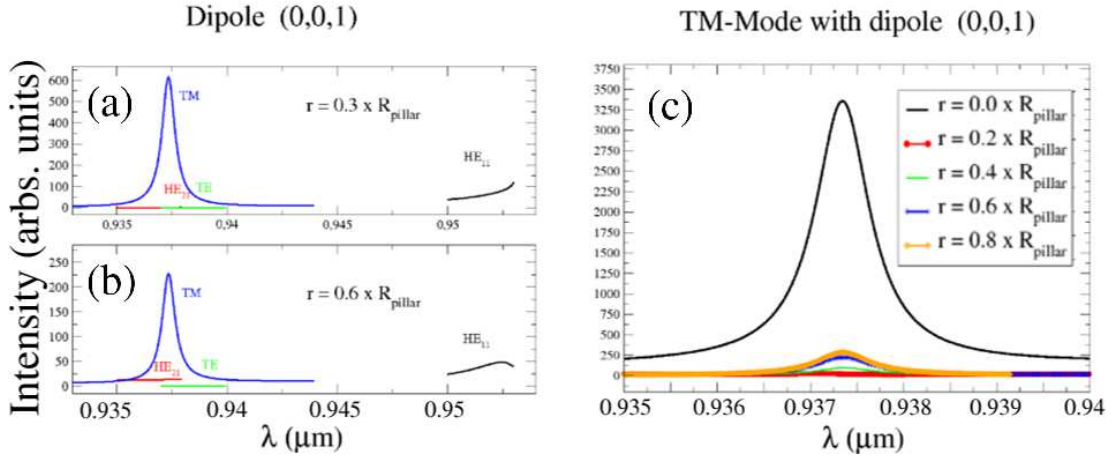
Figure 2.9: Dot dipole position and orientation effect over mode excitation intensity. Dipole with orientation $(0, 0, 1)$, located in $r = 0.3R_{Pillar}$ (a) and $r = 0.6R_{Pillar}$ (b). Radial variation of the TM-mode peak intensity for a dipole with $(0, 0, 1)$ orientation.

excited modes of lowest energy change with dot position and orientation inside the pillar. Figure (2.10) shows spectra for these modes and also the fundamental mode calculated for excitation by a dipole which is oriented in the plane of the cavity, for several radial positions inside the pillar. It is clear from the figure that the intensity of excitation varies significantly with dipole (dot) position. The effect of the orientation of the polarization of the exciting dipole is demonstrated in Figure (2.11), which shows

34

spectra for the four modes of lowest energy for two orientations of the dipole in the plane of the cavity Silva. et al. [17] investigated the emission of 33 nominally identical pillars with circular cross sections of 1.5 μm diameter. The fundamental mode in these samples shows an experimental full width at half maximum of (0.22 ± 0.05) nm, which corresponds to a Q around 4300. The 33 pillars investigated were selected from a set of 62 as those in which neither the fundamental nor the first three excited modes showed a splitting, which would be an indicative of deviations from circular symmetry. We also chose only pillars which had the fundamental mode emission wavelength inside a 0.22 nm range. We therefore can be reasonably sure of the circularity and regularity of our pillars, an assumption that was subsequently confirmed by scanning electron microscope images of some of the samples.
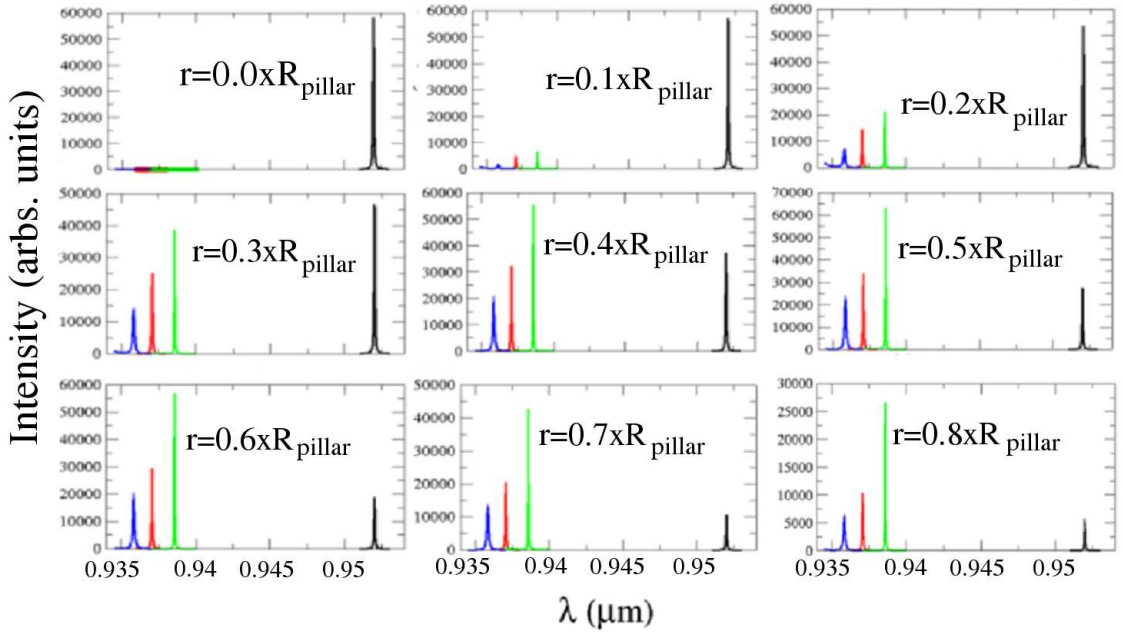
Figure 2.10: Theoretical spectra for a dipole $(1,1,0)$-oriented, i.e, a dot dipole with equal probability of emission in two orthogonal directions in the plane of the cavity and zero probability of an emission perpendicular to this plane.

Figure (2.12) shows representative spectra for the four lowest energy photonic modes
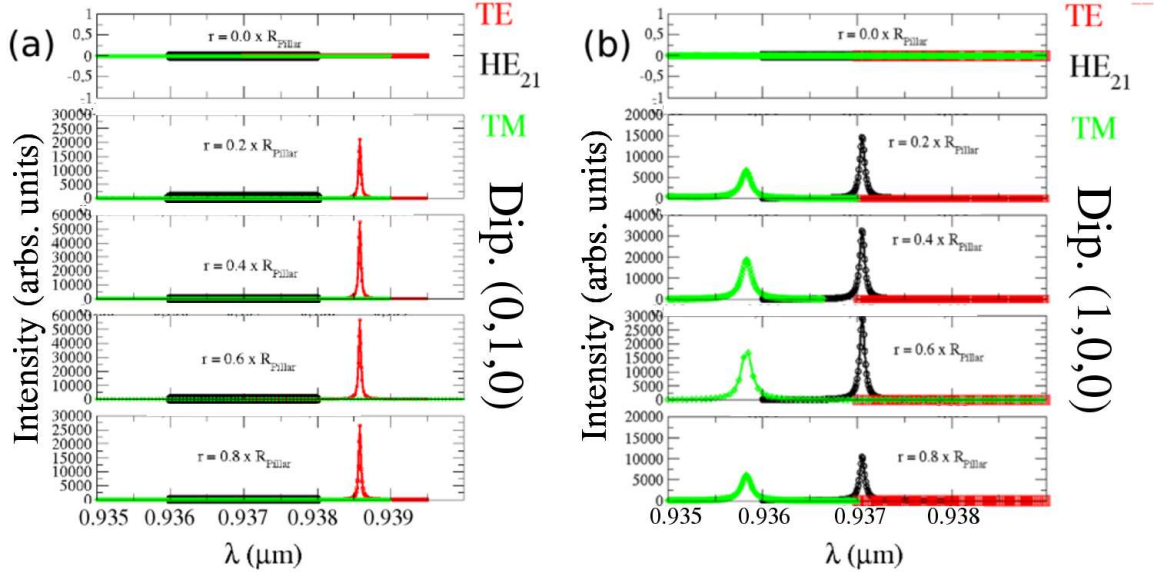
Figure 2.11: Comparison of spectra calculated for a dipole $(0, 1, 0)$-oriented and a dipole $(1, 0, 0)$-oriented, for $r = 0, 0.2R_{Pillar}, 0.4R_{Pillar}, 0.6R_{Pillar}$ and $0.8R_{Pillar}$.

of the 1.5 μm pillars. For all pillars, the fundamental HE11 mode is always the most intense but there is a clear distinction in the spectra concerning the relative intensities of the three higher energy modes. Of the 33 pillars investigated, 70% showed spectra similar to the one shown in Fig. (2.12-(a)), with the TE_{01} mode more intense than the HE_{21} while the TM_{01} is weaker. The TM_{01} mode is seen with relatively high intensity in only one sample (3%), shown in Fig. (2.12-(b)). The remaining 27% of the pillars showed spectra such as the one displayed in Fig. (2.12-(c)), with the HE_{21} as the most intense mode of the group of three excited modes.

The experimental spectra shown in Fig. (2.12) were reproduced using the CAMFR code (see Fig. 2.13) establishing the following conditions for the dot dipole:

Spectrum (a): Equal probabilities of excitonic dot emission in the X and Y directions, which can be identified with the [110] and [1$\bar{1}$0] crystalline directions. These directions are in the cavity plane perpendicular to the growth direction. The dot was located in $(r, \phi) = (0.3R_{Pilllar}, 0)$ where all modes

36

are intense enough and the coupling is good. But this is not the only way to reproduce this spectrum, e.g, if the dot is polarized along the X direction and is located in other position we can obtain the same result. This result can be better understood with reference to Fig. (2.13), which shows schematically the electric field profiles for the four lowest energy modes relative to the dipole, for two polarizations of the dipole in the plane (1,1,0).

Spectrum (b): This spectrum is a little complicated to reproduce due to the relative intensity of modes TM_{01} and HE_{21}. Only if the z component of the dot polarization is relevant enough the relative intensities shown in the experimental spectrum can be reproduced. This means that it is not possible to have TM_{01} more intense than HE_{21} without a considerable degree of Z-polarization. The theoretical spectra shown in Fig. (2.13-(b)) was obtained with polarization Y/Z=1 and X=60%Y.

Spectrum (c): In this case the relation between the components of the dot polarization taken was X=2Y and the dot is located in position 2 of Figure (2.13). The same kind of spectrum is obtained for a dot predominantly Y-polarized but located in position 1 or Figure (2.13).

All results discussed above imply that a large part of the quantum dots inside the pillar are polarized. This conclusion was verified from photoluminescence measurements at low power excitation, $\sim 1~\mu W$ [11], which showed experimentally that in a pillar that has a spectrum such as that shown in Figure (2.13)-(c) several dots are linearly polarized. The polarization is usually found to be along $[1\bar{1}0]$ with a degree of polarization as high as 90%. In the case of spectrum (2.13)-(b), determining if there are dots with z-polarisation well defined is difficult, since it would require lateral detection of the photoluminescence. Nevertheless, our theoretical results are an unmistakable evidence
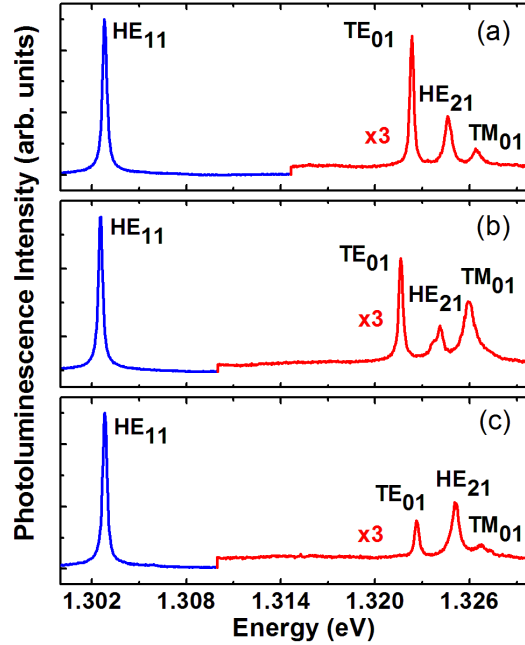
Figure 2.12: Experimental spectra for the set of 1.5 μm pillars studied. The spectra are normalized at the fundamental mode. The spectrum shown in (a) is characteristic of the major (70%) part of the samples, with TE_{01} mode as the most intense of the group of first three excited. In (b), although the TE_{01} mode is still of higher intensity, the TM_{01} mode is significantly excited, being more intense than HE_{21}. Only one (3%) pillar is in this category. The spectrum (c) is displayed by the remaining 27% of the samples.[Figure from ref. [17]].

of Z-polarization of the emission for the dots in these pillars. In conclusion, we showed that the relative intensities of the electromagnetic modes can be used to obtain information about the polarization of emission of quantum dots embedded in micropillars.

Summarizing all aspects treated in this chapter, by means of a relatively simple theoretical modelling we were able to understand some interesting results obtained for circular micropillars. These are structures which have been studied by many different groups in the world over the last years due to their several potential applications. We verify experimentally that the efficiency of excitation of the various photonic modes of the microcavity pillar depends significantly on the position and orientation of the quantum dot dipoles that act as the photon suppliers for the cavity allowed modes. It
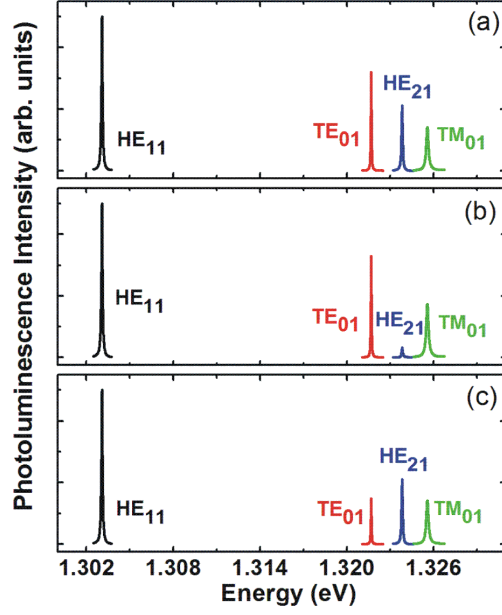
Figure 2.13: Calculated photoluminescence spectra for the 1.5 μm diameter micropillars. The PL spectrum in (a) is obtained with a dipole located in the horizontal axis, displaced 0.225 μm (0.3 times the pillar radius) from the center, with polarization in the plane with components X and Y of equal intensities. To obtain spectrum (b), the dipole is located 20°from the horizontal axis, 0.225 μm from the center. Its polarization has Y and Z components of equal magnitude and a X component which is 60% of the other two. For spectrum (c), the dipole is located in the horizontal axis, displaced 0.225 μm from the center, with polarization in the plane with components X and Y, with the Y component half the magnitude of the X component (See Fig. (2.14)).

was also showed that a large percentage of the dots in our pillar have a considerable degree of linear polarization, which has been experimentally confirmed. The analysis of the relative intensity of the photonic modes allows us to estimate the overall degree of in-plane polarization of the quantum dot ensemble and also to give information on polarization along the growth axis, a quantity which is usually difficult to measure.
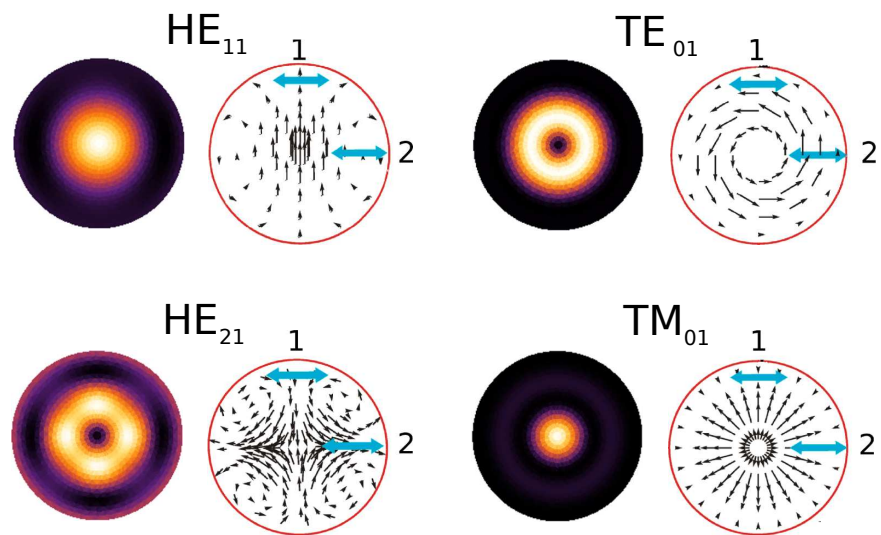
Figure 2.14: Flux lines and magnitudes of the Poynting vector of the four lower energy modes of a circular pillar in the plane of the cavity. The double arrows labeled 1 and 2 represent X-polarized quantum dot dipoles at two different positions in the cavity.

Chapter 3

Infrared Photodetectors

In this chapter, we present the basic ideas of the method proposed by Gangopadhyay and Nag [18] to calculate the energy levels of semiconductor structures with quantized momentum in one or more directions, as in the case of quantum wells, wires and dots, and more complex heterostructures used by specific technological applications such as photodetectors devices. Then we describe the implementation of this method to calculate the structures of our interest, namely, quantum dot infrared photodetectors, and describe the results obtained for a particular structure.

3.1   Description of the Method

In order to calculate the energy levels of this kind of system, we use the Schrödinger equation in the effective mass approximation with dimensionless units, given by:

$$-\left(\nabla \frac{m_e}{m^*(\vec{r})} \cdot \nabla\right) \psi(\vec{r}) + V(\vec{r})\psi(\vec{r}) = E\psi(\vec{r}), \tag{3.1}$$

with m_e the free-electron mass and $m^*(\vec{r})$ is the effective-electron mass in structure. We adopt the Rydberg $R_y = 13.6\ eV$ as the unit of energy and the Bohr radius $a_o = 0.529 \mathring{A}$ as the unit of length. In this way, energies obtained by solving (3.1) must be multiplied

by R_y and the lengths by a_o to get the real value.

To solve (3.1), $\psi(\vec{r})$ is expanded in a suitable set of functions which are solutions of a similar but less complex system. In other words, let $\hat{H}$ be a Hamiltonian operator of our system which can be separated as follows

$$\hat{H} = \hat{H}_o + \hat{V} \tag{3.2}$$

where $\hat{V}$ represents the potential of the system and $\hat{H}_o$ is the Hamiltonian of a simple problem which satisfies the eigenvalue problem

$$\hat{H}_o|g_i\rangle = E_i|g_i\rangle,$$

with $\{g_i\}$ being the set of functions in which any general function $\psi(\vec{r})$ will be expanded,

$$\psi(\vec{r}) = \sum_i a_i g_i(\vec{r}), \tag{3.3}$$

for $g_i(\vec{r}) = \langle\vec{r}|g_i\rangle$. We choose the system represented by $\hat{H}_o$ to be an electron with effective mass m_e confined in a large cylinder of potential $V_o = 0$, radius R and height L which is surrounded by air as it is shown in Figure (3.1).

To find $\{g_i\}$ we must solve the Schrödinger equation in cylindrical coordinates by separation of variables

$$g_{i\to l,m,n}(r, \varphi, z) = R_{lm}(r)\phi_l(\varphi)Z_n(z) \tag{3.4}$$

that generates the uncoupled system of equations
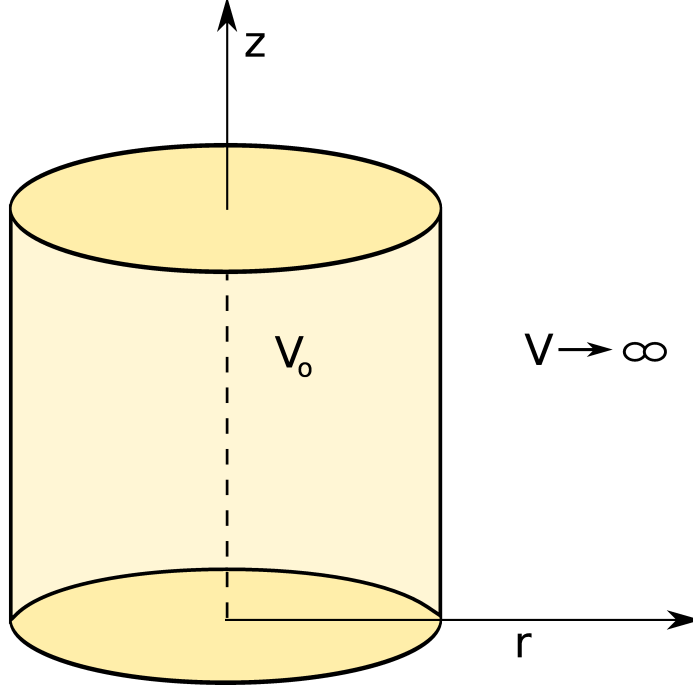
Figure 3.1: Physical system represented by $\hat{H}_o$, used to construct the basis to expand the wave functions.

$$\frac{d^2}{d\varphi^2}\phi_l + l^2\phi_l = 0$$

$$\frac{d^2}{dz^2}Z_n + \left(k^2 - l^2\right)Z_n = 0 \qquad (3.5\text{a})$$

$$\rho^2\frac{d^2}{d\rho^2}R_{lm} + \rho\frac{d}{d\rho}R_{lm} + \left(\rho^2 - \alpha^2\right)R_{lm} = 0$$

where $\rho = \alpha r$ and $k^2 = 2m_e E/\hbar^2$. By use of boundary conditions $g_{lmn}(r = R, \phi, z) = 0$ and $g_{lmn}(r, \phi, z = 0, L) = 0$, we have

$$R_{lm}(r) = \frac{\sqrt{2}}{RJ_{l+1}\left(k_{lm}\right)}J_l\left(k_{lm}\frac{r}{R}\right), \qquad (3.6)$$

$$\Phi_l(\varphi) = \frac{1}{\sqrt{2\pi}}e^{il\varphi}, \qquad (3.7)$$

$$Z_n(z) = \sqrt{\frac{2}{L}} sin\left(\frac{n\pi}{L}z\right). \tag{3.8}$$

with the orthonormalization condition given by

$$\int_V dV\, g^*_{l'm'n'} g_{lmn} = \delta_{l'l}\delta_{m'm}\delta_{n'n}. \tag{3.9}$$

The energies levels for this problem are

$$E_{lmn} = \frac{\hbar^2}{2m_e}\left(\frac{n^2\pi^2}{L^2} + \frac{k^2_{lm}}{R^2}\right),$$

with k_{lm} the m-zero of the Bessel function of order l. With this set established, we are going to study the problem of a quantum dot embedded in a cylinder like the one described above. For this, we need to solve the eigenvalue equation

$$\hat{H}|\psi\rangle = E|\psi\rangle,$$

where $\hat{H}$ contains all information about the quantum dot and barriers (mass and potential). So, if we replace equation (3.3) into (3.1), multiply this by $g^*_{l'm'n'}$ and integrate over all space, we obtain the characteristic equation

$$A_{l'm'n',lmn} - E\delta_{l'l}\delta_{m'm}\delta_{n'n} = 0, \tag{3.10}$$

where by use of integration by parts, boundary and orthonormalization conditions for the g_i-functions, we have

$$A_{l'm'n',lmn} = -\iiint_{space} dV\left(g^*_{l'm'n'} \cdot \frac{m_e}{m^*}\nabla^2 g_{lmn} - g^*_{l'm'n'} V g_{lmn}\right). \tag{3.11}$$

It is possible to reduce this expression integrating by parts the left term in the parenthesis, so we finally obtain

$$A_{l'm'n',lmn} = -\iiint_{space} dV \left(\frac{m_e}{m^*} \nabla g^*_{l'm'n'} \cdot \nabla g_{lmn} - g^*_{l'm'n'} V g_{lmn} \right). \tag{3.12}$$

In order to solve this analytically, we must note that there is a spatial dependence of the effective mass, i.e., the structures studied here have discontinuous effective mass and potential functions in the interfaces between two different materials. To overcome this problem, the integral (3.12) is split into three parts:

(a) We integrate (3.12) with $m^*(r, z) = m_b$ and $V(r, z) = V_b$ over all space, i.e., over the external cylinder because $\psi = 0$ in the boundaries of this (see Fig. 3.2). The result of this is

$$\left[A^{Cyl}_{l'm'n',lmn} \right]_{m_b,V_b} = \left(\frac{m_e}{m_b} \left(\frac{k^2_{lm}}{R^2} + \frac{n^2 \pi^2}{L^2} \right) + V_b \right) \delta_{l'l} \delta_{m'm} \delta_{n'n}.$$
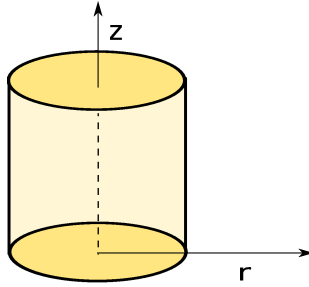
Figure 3.2: Model of the cylinder used to generate the basis of functions for the problem.

(b) Then, in the last term we subtract the integral over the region where the quantum dot is located with $m^*(r, z) = m_b$ and $V(r, z) = V_b$, and afterwards we add the same integral but with the right parameters, i.e, $m^*(r, z) = m_{QD}$ e $V(r, z) = V_{QD}$ (see Fig. 3.3), that is

$$\left[A_{l'm'n',lmn}^{QD}\right]_{m_b,V_b} - \left[A_{l'm'n',lmn}^{QD}\right]_{m_{QD},V_{QD}}$$

$$= \iiint_{QD} dV \left(\frac{m_e}{m_{QD}} - \frac{m_e}{m_b}\right) \nabla g_{l'm'n'}^* \cdot \nabla g_{lmn}$$

$$+ \iiint_{QD} dV (V_{QD} - V_b) g_{l'm'n'}^* g_{lmn} \quad (3.13)$$
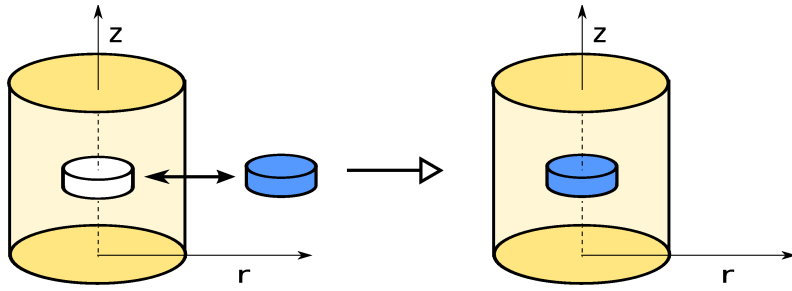
Figure 3.3: An illustration of the process to include the quantum dot potential.

(c) Finally, the matrix element A is given by

$$A_{l'm'n',lmn}^{Total} = \left[A_{l'm'n',lmn}^{Cyl}\right]_{m_b,V_b} + \left[A_{l'm'n',lmn}^{QD}\right]_{m_b,V_b} - \left[A_{l'm'n',lmn}^{QD}\right]_{m_{QD},V_{QD}}$$

(d) In this way, it is possible to generalize this process to deal with a more complex structure that combines quantum dots and quantum wells, which is our objective in this work. So, if the structure consists of N dots and M wells, the matrix element is

$$A_{l'm'n',lmn}^{Total} = \left[A_{l'm'n',lmn}^{Cyl}\right]_{m_b,V_b} + \sum_{i=0}^{N} \left(\left[A_{l'm'n',lmn}^{QD_i}\right]_{m_b,V_b} - \left[A_{l'm'n',lmn}^{QD_i}\right]_{m_{QD_i},V_{QD_i}}\right)$$

$$+ \sum_{i=0}^{M} \left(\left[A_{l'm'n',lmn}^{Well_i}\right]_{m_b,V_b} - \left[A_{l'm'n',lmn}^{Well_i}\right]_{m_{Well_i},V_{Well_i}}\right). \quad (3.14)$$
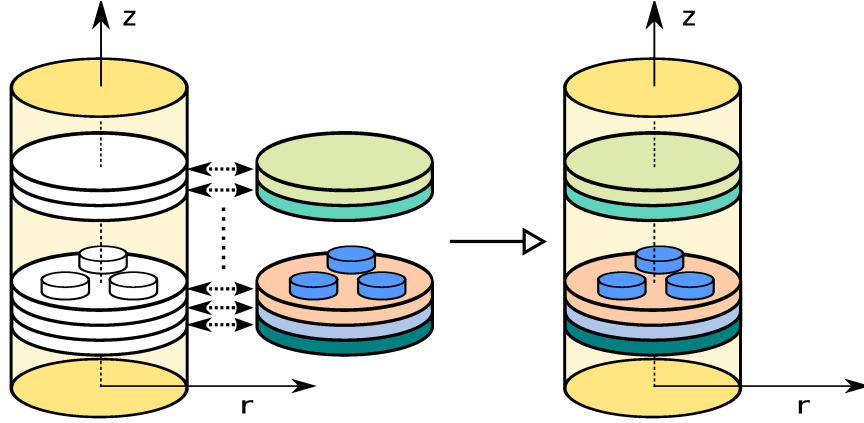
Figure 3.4: Illustrating the process of adding the potential of a few quantum dots and other layers.

Here the notation $[A]...$ represents the integrals (3.12) over regions and parameters of interest. In the last figures we assume that the quantum dots shape is a small cylinder, but this is not necessary, the algoritm exposed is general, i.e, the quantum dot shape can be changed arbitrarily and the logic of the method is preserved, as it will be shown in the next section.

3.1.1 Introducing Quantum Dots with Different Shapes

So far, we only presented how to solve the matrix elements for an arbitrary structure. In this section we focus our efforts in order to show how the quantum dot shape is included in the solution of (3.14), because it is known that this shape varies, depending on the growth process, and is affected by the strain caused by the differences between the lattice constants of the substrate and the material of which the quantum dot is fabricated. For this, we go back to equation (3.13) to solve the triple integrals, where by a careful use of upper and lower integral limits it is possible to change the dot shape as follows

$$\iiint_{QD} dV \nabla g^*_{l'm'n'} \cdot \nabla g_{lmn} = \int_0^{R_o} dr \, r \left(\frac{d}{dr} R^*_{l'm'} \frac{d}{dr} R_{lm} + R^*_{l'm'} R_{lm} \right) S_{n'n}(z(r)) \delta_{l'l}$$

$$\text{(3.15)}$$

$$+ \frac{\pi^2 l' l}{L^2} \int_0^{R_o} dr \, r R^*_{l'm'} R_{lm} C_{n'n}(z(r)) \delta_{l'l}$$

for

$$S_{n'n}(z(r)) = \int_{z_d}^{z(r)} dz \, Z^*_{n'} Z_{n'}$$

$$C_{n'n}(z(r)) = \int_{z_d}^{z(r)} dz \, \frac{\partial}{\partial z} Z^*_{n'} \frac{\partial}{\partial z} Z_{n'}$$

where we used

$$\int_0^{2\pi} d\phi \, \varphi_{l'}(\phi) \varphi_l(\phi) = \delta_{l'l}. \tag{3.16}$$

Let us note that the function $z(r)$ in the upper limit describes how the dot-shape is in the rz-plane and due to azimuthal simmetry a revolution surface created by rotation of this plane about the growth direction gives us the desired dot. For a desired non-symmetric dot shape the ϕ-dependence is not the same as before, in this case the best procedure is to change the set of functions which is solution of $\hat{H}_o$ for other more convenient set that has the geometrical properties of the dot shape, as in the case of a pyramidal dot with square base. Figure (3.5) shows some shapes with azimuthal simmetry for which the development made here is totally applicable.

In this way, the formulae for these shapes are:

48
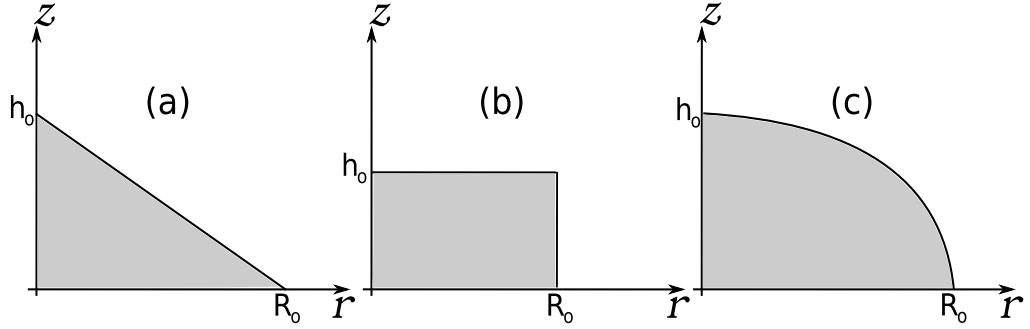
Figure 3.5: (a) Cone-shaped quantum dot (b) cylinder-shaped quantum dot and (c) lens-shaped quantum dot.

1. Cone-Shaped QDs:

$$z(r) = h_o \left(1 - \frac{r}{R_o} \right) \tag{3.17}$$

2. Cylinder-Shaped QDs:

$$z(r) = \begin{cases} if \ 0 \leq r \leq R_o, \ h_o \\ otherwise, \ 0 \end{cases} \tag{3.18}$$

3. Lens-Shaped QDs:

$$z(r) = h_o \sqrt{1 - \frac{r^2}{R_o^2}} \tag{3.19}$$

Other sorts of quantum dot shapes can be designed by changing the upper limit of 2π to a function $\phi(r)$.

3.2 Strain and deformation Conduction Band

One of the most important effects that affects considerably the energy levels in a self-assembled quantum dot is the strain caused by the difference between the lattice constants of the materials involved. The strain modifies the energy gap of each one and therefore the conduction (valence) band profile is also changed. This strain in a general view propagates in the first atomic planes and along the growth direction as it is shown

schematically in the figure (3.6).
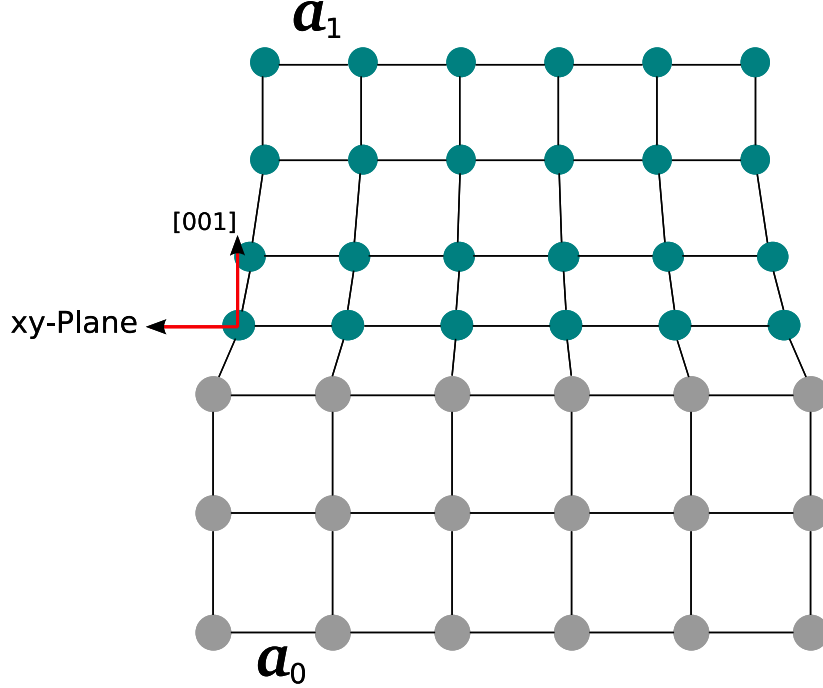
Figure 3.6: Strained heterostructure scheme showing that the strain propagates in the first atomic planes and along the growth direction.

This is an example of a biaxial strain, which is the most common kind of strain in these heterostrutures. Mathematically this phenomenon can be modelled by means of a symmetric tensor e_{ij} that describes the strain induced in the crystal by the atomic displacements ($\mathbf{R}$) and is known as the **strain tensor** [49] defined by

$$e_{ij} = \frac{1}{2}\left(\frac{\partial \delta \mathbf{R}_i}{\partial \mathbf{R}_j} + \frac{\partial \delta \mathbf{R}_j}{\partial \mathbf{R}_i}\right). \tag{3.20}$$

With the use of group theory and the above definition of e_{ij}, it can be shown that the trace of this tensor is equal to the fractional volume change ($\delta V/V$) associated with a strain pattern, and which gives the energy shift suffered for an electronic structure as follows

$$\delta E_{nk} = a_{nk}\delta V/V, \tag{3.21}$$

with a_{nk} defined as the **volume deformation potential** of the energy E_{nk}. So, we have that the correction in the potential operator $\hat{V}$ is given by

$$V_{strain} = a_c(e_{xx} + e_{yy} + e_{zz}), \tag{3.22}$$

and so, the conduction band edge becomes

$$E_{CB} = \frac{\hbar^2}{2m_e}k_z^2 + E_g + V_{strain}. \tag{3.23}$$

The biaxial strain components for [001]-oriented structures, as given by [9], are

$$e_{xx} = e_{yy} = e_{\parallel} = \frac{a_s - a_m}{a_m}, \tag{3.24}$$

$$e_{zz} = -2\frac{C_{12}}{C_{11}}e_{\parallel}, \tag{3.25}$$

where a_s and a_m ase the lattice constants of the substrate and epilayer materials, which are zinc-blende (cubic) crystals, and C_{11} and C_{12} are the stiffness constants in the strained epilayers [37].

3.2.1 Practical Examples

Now we use a simple structure to present how to merge this method and we present some results obtained. Consider a InAs-quantum dot embedded in InP. In the figure (3.7) we show how the conduction band edge profile is built where the equation (3.23) is used for $k_z = 0$ (gamma point), and the values of valence band offset (VBO) of each material are taken with respect to the alloy common axis, and the other parameters as effective masses, energy gaps, lattice constans, stiffness constants are computed using

the formulae established in the reference [45]. The conduction band profile for the strained structure in Figure (3.7), along the growth direction, is given by

$$V(z) = \begin{cases} 0.2398 \ eV, \ if \ 0 \le z \le a \ and \ z > b \\ 0, \ if \ a \leqslant z \leqslant b \end{cases} \tag{3.26}$$
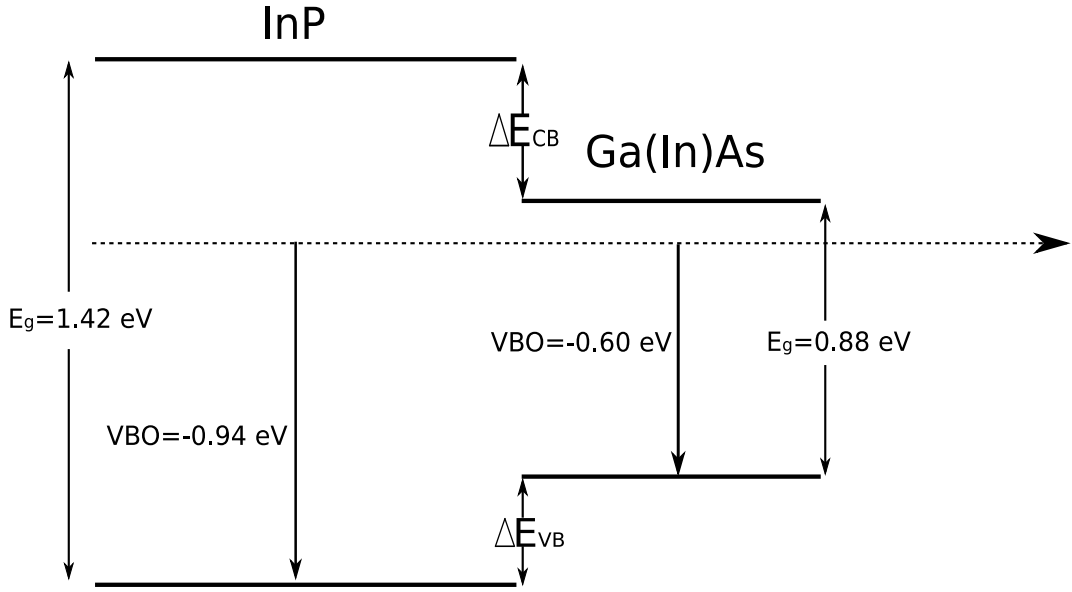
Figure 3.7: Band offset scheme for InAs quantum dots grown onto InP.

which is computed using equation (3.23) and the effective masses are $m_{InP} = 0.0795 m_e$ and $m_{GaInAs} = 0.0455 m_e$. As it was shown previously we can change the quantum dot shape with an unidimensional function $z(r)$, in this way we choose three particular shapes: a cylinder, a truncated cone and a cone, all with circular base. In Figure (3.8) it is shown the convergence of the method is shown for these three dot shapes, where it is possible to see how big is the basis dimension we must take to obtain reliable energy levels and the real behavior of the wave functions, and from these obtain the inter-sub-band transitions, which is our objective.

Here, we use for the quantum dot the parameters, defined in Figure (3.8), $h_o = 10 \ nm$, $R_o = 10 \ nm$ and $r_o = 5 \ nm$, which are the height, major and minor radii, respectively.
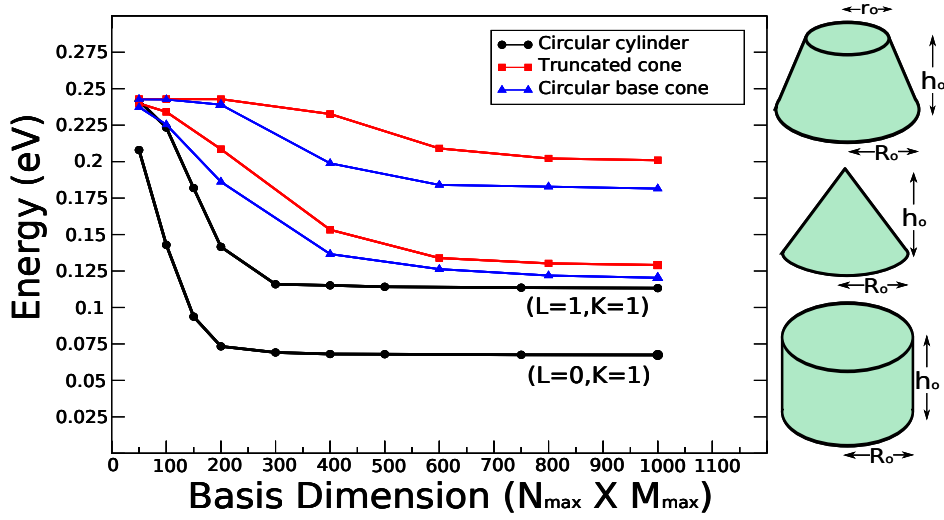
Figure 3.8: Convergence of the method. The dependence of two energy levels, indexed by the quantum numbers L and K (see text) are shown as a function of basis dimension for different dot shapes:(*Black*) Circular cylinder, (*Blue*) circular base cone and (*Red*) Circular truncated cone.

In order to build the basis to expand the wave functions of the dots, we have three parameters $\{l, m, n\}$ to increase until the convergence is obtained. Due to azimuthal symmetry the l-values are decoupled and these can be worked separately. Therefore the wave functions can be labeled as

$$\psi_{l,k}(r, \varphi, z) = \sum_{mn} a_{mn}^l g_{lmn}, \tag{3.27}$$

and the basis dimension is given by $dim = N_{max} \times M_{max}$, where N_{max} and M_{max} are the values for which the convergence is obtained. In the current case, $N_{max} \geq 50$ vertical and $M_{max} \geq 16$ lateral functions were taken. Obviously, this dimension size changes depending on the structure built, because adding wells, wetting layers, dots and other layers modifies the electronic energies computed. But normally $N_{max} = 200$ and $M_{max} \geq 10$ is enough to achieve good convergence. The outer cylinder dimensions must be taken such that they do not affect the electronic levels of the quantum dots. We take a ratio $R/Ro = 6$.

Figure (3.9) shows the lowest energy levels and respective wave functions for cylinder, truncated cone and cone dot shapes. It is possible to see what is the effect when the dot shape is changed, for example, the ground state is shifted up a few meV's and fifth energy levels are shifted up to the continuous, all this mainly due to quantum dot size being reduced and thus the confinement increased. An interchange in the order between the third and the fourth energy levels is also noted and that only the ground state wave functions preserve the symmetry respect to the center of the conduction band offset, which is due to the fact that the symmetry of the dot shape in the zr-plane is broken. It is expected that this effect is increased when the dot size is smaller as in the case of the circular cone dot shape. The wavefunctions behavior along the growth direction are computed near $r = 0$ because $\psi_{l,k}(0, \varphi, z) = 0$ for $l > 0$.
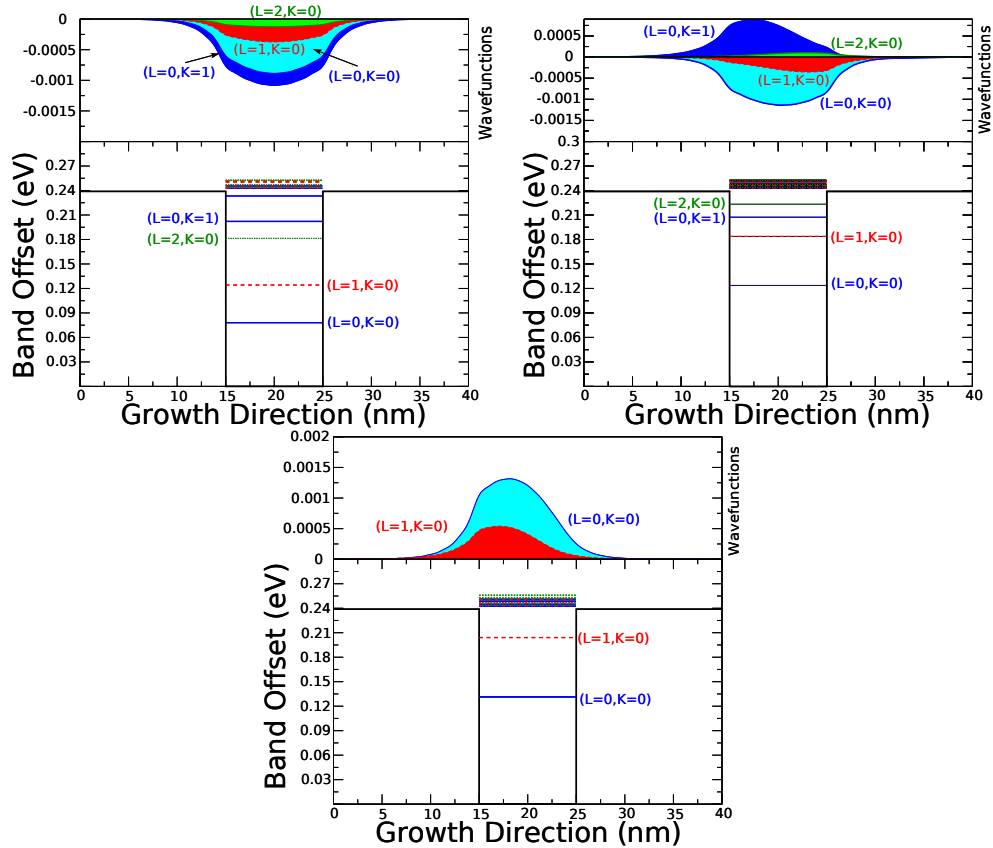
Figure 3.9: The lowest energy levels and wavefunctions for (a) cylinder, (b) truncated cone and (c) cone dot shape.

It is also possible to modify the potential to study the effect caused by a electric field applied to the structure. For this purpose, we introduce the potential

$$\Delta V = -E_{field}\, z, \tag{3.28}$$

in equation (3.23). The immediate effect is to tilt the conduction and valence bands either in a positive or negative form, depending on the direction the electric field is applied. In Figure (3.10) we show how the probability densities behavior $|\psi_{l,k}|^2$ under a voltage applied for a GaAs/AlGaAs quantum well, which are not symmetric respect anymore to the center of quantum well, as in the case without *bias* and, as expected, the distribution density for the ground state is right-shifted. The energy levels also suffer a down-shifting due to the confined Stark effect. In the next section we present how it is possible to introduce other kinds of potentials in order to get a more realistic system.
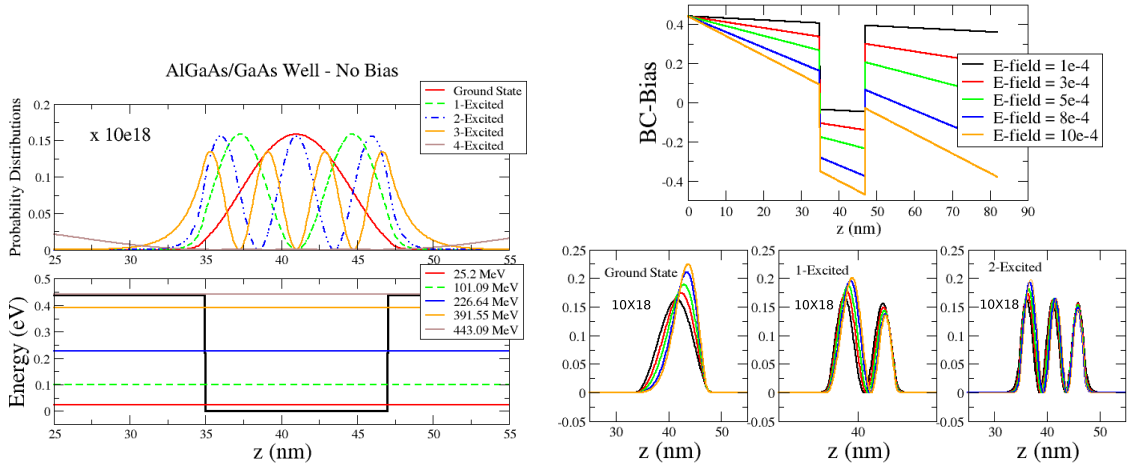
Figure 3.10: (*left*) GaAs/AlGaAs quantum well energy levels and probability densities. (*right*) Effect *bias* potential over same system. It is note the shifting of probability densities.

3.3 Some Corrections to the Model

So far, we focused our attention in the main contribution, CB(VB) potential profile at the Γ point, that needs to be considered in order to solve the single-particle Schrödinger

equation in order to find the energy levels configuration of the structures studied here. However, there are additional interacitons that correct these energies to more realistic values. Here we will present the most relevant of these and expose criteria for when they need to be taken into account.

Let us begin with the *Coulomb interaction*, which is responsible for the asymmetries between the forward and reverse I-V characteristics of QWIP's systems. The segregation of the Si dopant atoms occurs during growth leads to an asymmetry in the doping profile and hence in the potencial $\hat{V}$, which, for instance, can be modeled in one dimension as follows

$$V(x) = \frac{e^2}{\epsilon} \int_{-\infty}^{x} dx_1 (x - x_1)[N_D^+(x_1) - n_{2D}\psi^*(x_1)\psi(x_1)], \qquad (3.29)$$

which satisfies the Poisson equation:

$$\frac{d^2}{dx^2}V = [N_D^+(x_1) - n_{2D}\psi^*(x_1)\psi(x_1)]. \qquad (3.30)$$

This equation assumes that all dopants are ionized, so that $\int_{-\infty}^{\infty} dx N_D^+(x) = n_{2D}$; the ψ are the wavefunctions of the problem without Coulomb interaction. When the potential profile is modified, both energies and wavefunctions also change, and a change in the wavefuntion implies that the potential profile also changes. This is a self-consistent process which solution is obtained by solving numerically the Poisson and Schrödinger equations, that will be stopped as convergence is achieved. The corrections to the approximate model are reported in the literature [42, 22] and these are of the order of $1 - 2$ %, even with higher or uniform doping in the system, because the spread out of the ionized dopand charges mostly balances the carrier charge determined by the wavefunction shape.

The inclusion of the last correction leads us to think in the *Many-Particle Effects* as another correction to be implemented. For this purpose, we must remember that electrons and holes are spin-1/2 particles obeying the Fermi statistics and the Pauli exclusion principle, therefore the wavefunction for N particles must be anti-symmetric and it is given by a Slater determinant. The correction to first-order of the energy in the perturbation theory will involve terms concerning to direct Coulomb interaction and "exchange" correction, which does not have classical analogy. Another way to compute the energy correction is the so-called Hartree-Fock equation, which is based in the mean field theory with the Coulomb interaction and the exchange as corrections. The discussion done in this work uses the simple single-particle Schrödinger equation, but our potential profile is obtained from the lowest and highest points in the band structure, for the conduction and valence band respectively; it means that the bands are parabolic according to the wavevector dispersion relation. One of the most usual corrections implemented in this kind of system is, is to consider variations in that parabolicity, in other words, the non-parabolicity of the bands plays an important role, which is commonly treated by $k \cdot p$ formalism [49]. In the $k \cdot p$ the non-parabolicity is explained by the mixing of the conduction band with additional bands. For example, the 8-band $k \cdot p$ model, originally proposed by E. O. Kane [27], uses an 8×8-matrix Hamilton operator acting on the wavefunctions of electron, heavy-hole, light-hole, and split-off bands, each with two spin values.

Introducing this kind of corrections is not in the scope of this work because we are interested in single-particle transitions in order to understand the photodetection processes in infrared photodetectors. For this aim, the method described above is a good approximation to the results obtained in the many-particle theory. In principle, Coulomb interaction can be introduced relatively easy in our numerical diagonalization process, but for the other corrections it would be better to use other methods.

3.4   Oscillator Strength

The oscillator strength is a parameter that allows us to know which are the most probable transitions in the system, either inter-band or inter-sub-band transitions, due to absorption of incident radiation. To compute this parameter the most frequently used formula is

$$f(l', k'; l, k) = \frac{2m^*}{\hbar^2} \left(E_{l',k'} - E_{l,k} \right) |\langle l', k' | \vec{r} | l, k \rangle|^2. \tag{3.31}$$

Its use depends on the system of units used, but what is really important are the relative values between the transitions. The difficulty in this point is to calculate the matrix element of position vector $\vec{r}$. In our case we have that

$$\begin{aligned}
\langle l', k' | \vec{r} | l, k \rangle &= \int_V d\vec{r} \, \langle l', k' | \vec{r} | \vec{r} \rangle \langle \vec{r} | l, k \rangle \\
&= \int_V d\vec{r} \left(x\hat{i} + y\hat{j} + z\hat{k} \right) \langle l', k' | \vec{r} \rangle \langle \vec{r} | l, k \rangle \\
&= \int_V d\vec{r} \left(x\hat{i} + y\hat{j} + z\hat{k} \right) \psi_{l',k'}^*(r, \varphi, z) \psi_{l,k}(r, \varphi, z) \tag{3.32}
\end{aligned}$$

where $\langle \vec{r} | l, k \rangle = \psi_{l,k}(r, \varphi, z)$ are the eigen-functions of our problem. In Table (3.1), we show some values of oscillator strength calculed for an InAs/InP quantum dot.

In the next section, we present the result of a study of quantum dot infrared photodector device structure in order to explain some experimental results.

(l', k')	$\Delta E(l', k'; l, k)$	(l, k)	$f(l', k'; l, k)$
0 0	(0.11750 eV)	0 1	1.552704
0 0	(0.16854 eV)	0 2	68.330235
0 0	(0.19550 eV)	1 1	0.355176
0 0	(0.20816 eV)	1 2	0.313632
0 1	(0.13944 eV)	0 5	39.380838
1 0	(0.16682 eV)	1 2	23.066503
1 0	(0.18974 eV)	1 3	0.165258
1 1	(0.10396 eV)	1 6	26.993308
1 1	(0.13550 eV)	1 7	30.007537
1 1	(0.16501 eV)	1 8	3.277813
1 1	(0.20378 eV)	1 9	5.288124

Table 3.1: Oscillators strength for an InAs-quantum dot with height 9 nm and radius of 15 nm embedded in InP with wetting layer.

3.5   Results

Now, we present the numerical results obtained for the sample shown schematically in Figure (3.11). The experimental measurements were made by **PhD student Déborah Reis Alvarenga** from Universidade Federal de Minas Gerais, Brazil. A C-code was built in order to implement the method exposed above sections. This code uses the GNU Scientific Libraries (GSL) and paralleling libraries MPI. A detailed introduction about the use of this code, is presented in the Appendix.

The sample of our interest here is a combination of a cylinder-shaped InAs quantum dot(s) with height 7 nm and diameter of 43 nm, and a InGaAs quantum well of width 10 nm, separated by a thin barrier of $Al_{0.16}Ga_{0.31}In_{0.53}As$ of width 3 nm. This barrier is included because the density of self-assembled dots grown over it is high compared with the density of dots that grow over InGaAs, therefore, a desirable characteristic for a good infrared detector. The InP-barrier is strongly linked to the final dot shape due to the strain in this heterojunction and the diffusion/segregation of In during the growth process. In our sample, Transimission Electron Microscope images done by *Sandra M.*
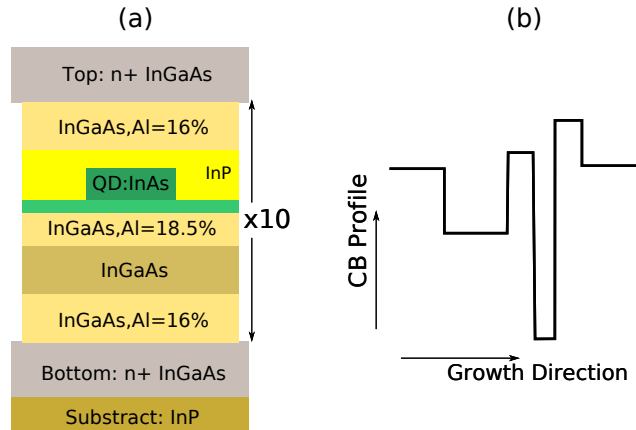
Figure 3.11: Design of a period of the sample (a). Conduction band profile scheme of the sample (b).

Landi in INMETRO show that the dot shape is approximately a cylinder, which facilitates the calculation of the energy levels in the diagonalization process. The final device consists of 10 repetitions of this period, which is grown over an InP substrat. Lower and upper contact layers of n-doped of InGaAs are also grown, in order to collect the photocurrent resulting from the photodetection proccess.
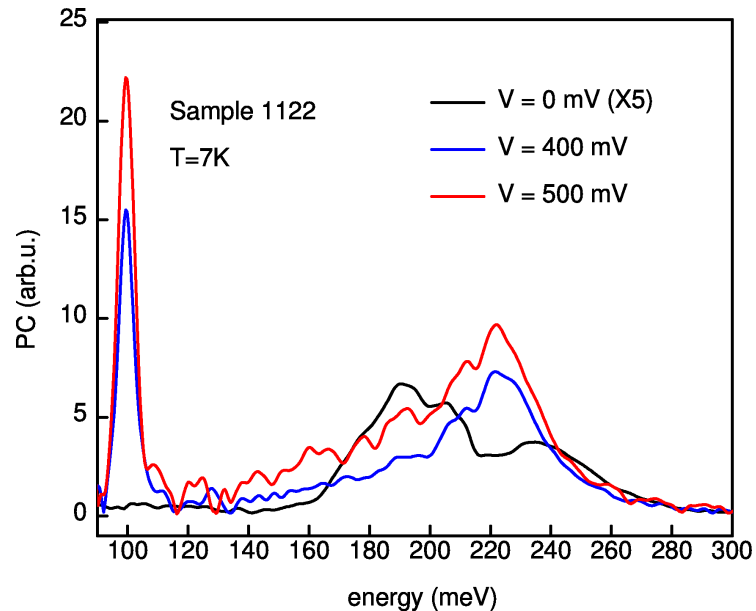
Figure 3.12: Experimental photocurrent spectra. Response peaks are observed in various energy regions indicating photodetection.

Figure (3.12) shows the experimental photocurrent spectra measured for the sample described above. The measurement was made at $T = 7\ K$ for several applied positive *biases*, we show the experimental spectra for $V_{bias} = 0, 400$ and $500\ mV$. We note that there exists a relatively sharp peak $\sim 100\ meV$, which is interesting for applications that require sensors working at $\sim 12\ \mu m$ (see Chap. 1). Note that this peak does not appear for $V_{bias} = 0$.

In the range between $160 - 260\ meV$, we note other much broader peaks, which are seen, even for $V_{bias} = 0$. In order to assign the observed photocurrent peaks to transitions in the structure, we used the above described method to calculate the energy levels and oscillator strengths to the optical transitions between these. The calculated energy levels are shown schematically in Figure (3.13). The levels can be classified according to the angular number L. It is interesting to note that the Hamiltonian for this system can be diagonalized independently for each L, since there is no matrix element linking states with different L, as can be demonstrated by calculating equation (3.14).

An important fact to take into account is to note that for each angular momentum L we have a few quantum dot-like levels as expected, and a great quantity of levels that belong either to the quantum well or to the uppermost set of excited quantum dot energy levels, or that are a mixture of the latter two. Some of these levels are part of the wetting layer electron states, which are important since these levels can be understood as "mediator"-levels that allow to connect the states of the quantum dot and those of quantum well. The higher energy states can be the final states for the optical transitions due to the absorption of one or two photons, and so, when the *bias* is turned on, the electrons can be dragged across the structure contributing to the photocurrent. Figure (3.14) shows the densities of probability in rz-plane for the wavefunctions corresponding to the most probable optical transitions.

61
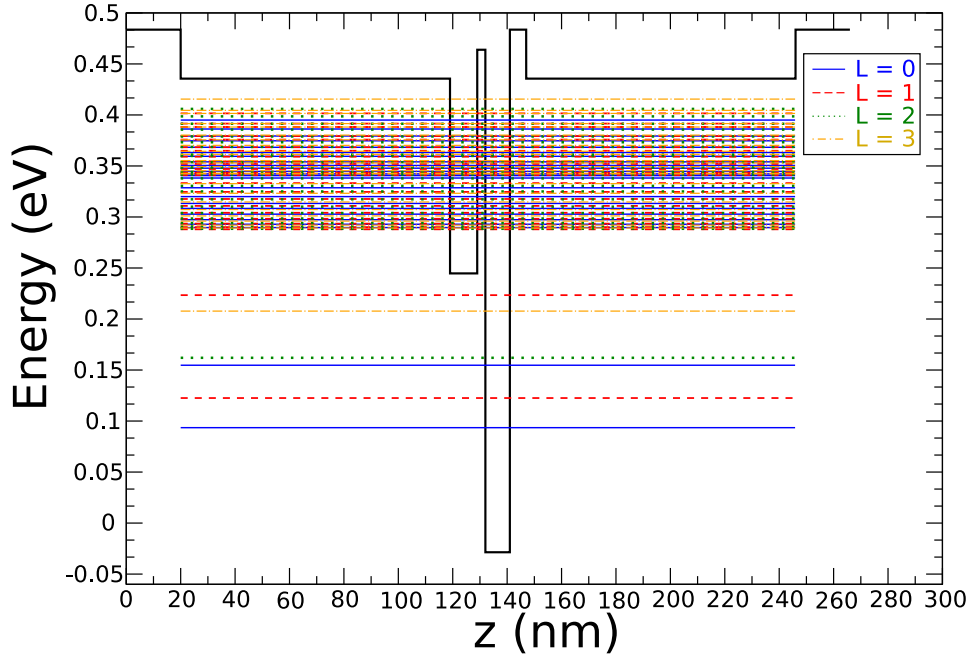
Figure 3.13: Energy levels scheme for sample shown in Fig. (3.11) with a cylinder-shaped quantum dot of height 7 nm and diameter 43 nm.

The green lines in Fig. (3.14) represent the interfaces between the different parts of the heterostructure. Along the growth direction, z, are shown the quantum well and quantum dot regions, the only regions where it is possible to have bounded states. We can see how the ground state $(L = 0, K = 0)$ and the first excited states are highly located in the quantum dot. It is also possible to see the quantum well states, which present small oscillations along the r-direction due to the fact that the electrons are free to move there, since there is no radial confinement. Note that electrons in these levels have a small probability to be in the dot region as in the case of $(L = 0, K = 10)$ and $(L = 0, K = 21)$, which would favour the optical coupling of these with lowest quantum dot states. The most particular of these states is $(L = 1, K = 24)$. An electron that is optically excited to this state has a high probability to be found in the quantum well region, and since it is relatively close to the continuum of states of the conduction band, it can also contribute to the current at low applied *biases*.
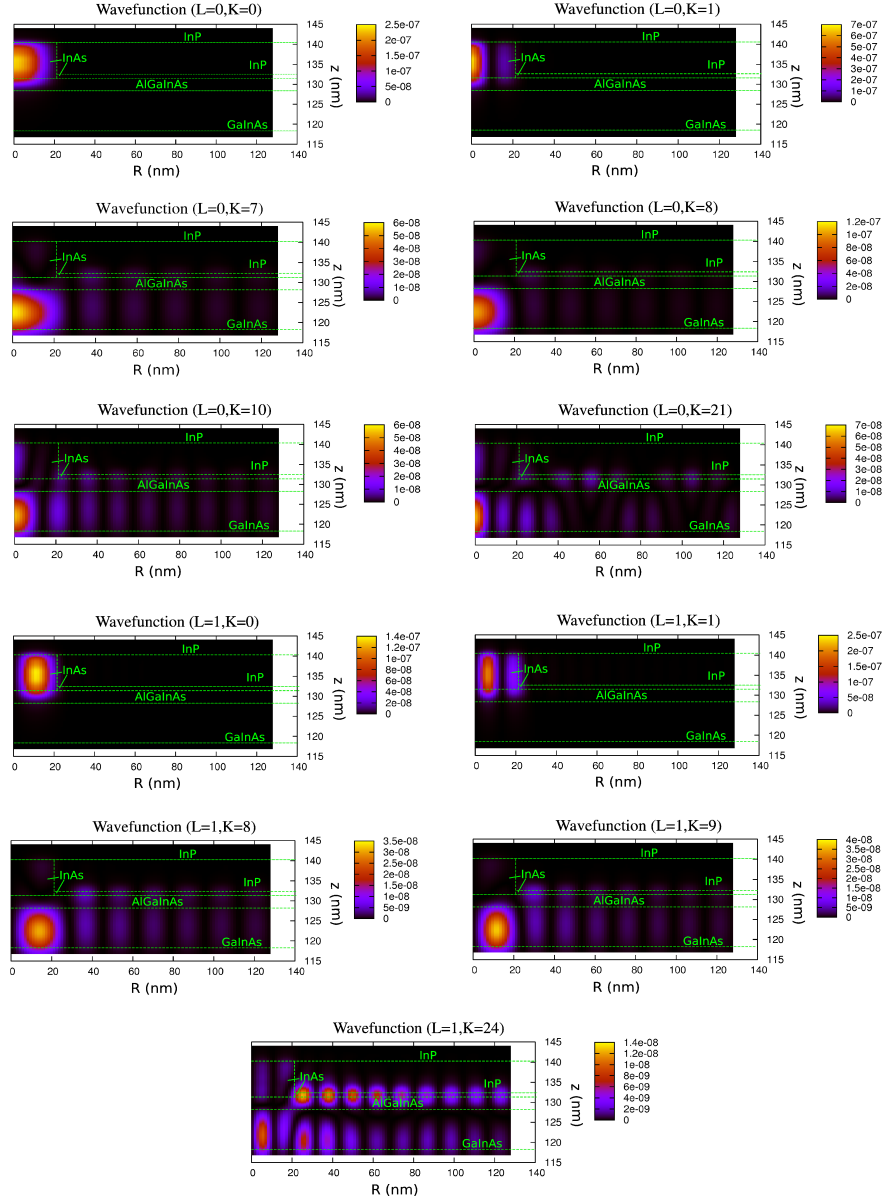
Figure 3.14: Densities of probability ($|\psi_{L,K}|^2$) in rz-plane for the wavefunctions corresponding to the most probable optical transitions. Regions corresponding to different materials are bounded by green lines.

In order to identify the optical transitions seen experimentally (Fig. 3.12), we calculated the oscillator strengths of all transitions starting from the lowest energy levels in the photodetector structure. In Figure (3.15) we show the transitions which have higher probability. Note that transitions from the lowest quantum dot levels to the quantum

well levels are strong, because the barrier between quantum well and quantum dot is thin, and the electron can tunnel easily between the two. The theoretical results predict the existence of a strong absorption due to an optical transition from the first excited state $(L = 1, K = 0) \rightarrow (L = 1, K = 1)$, with an energy $\sim 100\ meV$, in which L is preserved. This result is in good agreement with the experimental PC spectra obtained (see Fig. 3.12). Similarly, a second transition from $(L = 1, K = 1) \rightarrow (L = 1, K = 24)$ with an energy $\sim 178\ meV$ is also predicted. This transition is not clearly seen in the experimental spectra although it is likely that it is hidden inside the broad peak at 190 meV at zero *bias*. we propose that the $(L = 1, K = 0)$ to $(L = 1, K = 24)$ transition is directly related to that peak close to 100 meV. In our low samples only the three first quantum dot levels should be occupied at low temperatures. In this way, the PC peak seen at $\sim 100\ meV$ could be a two photon absorption process, as follows

$$(L = 1, K = 0) \xrightarrow{\hbar\omega_1} (L = 1, K = 1) \xrightarrow{\hbar\omega_2} (L = 1, K = 24)$$
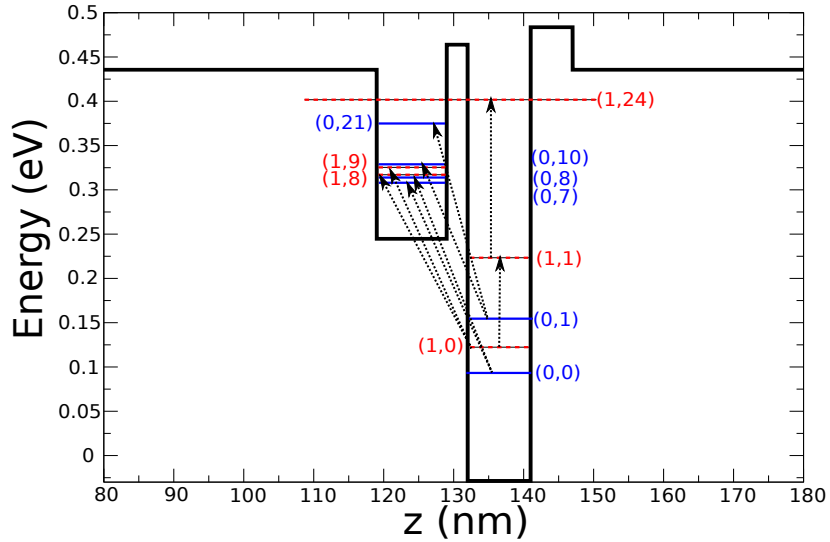
Figure 3.15: Relevant optical transitions in the system, i.e, the transitions with highest quantified by the oscillator strength f which have as initial state the three lowest energy levels of the structure.

This peak does not exist for negative *bias*. This fact can be understood because of

the existence of the InP-barrier of width 13 nm, and from the density of probability mapping for $(L = 1, K = 24)$ state, which shows us that it is more probable to find the electron to left.

(L, K)	(L', K')	f	$\Delta E(L', K'; L, K)$
0 0	0 7	27.44	214.87 meV
1 0	1 8	20.93	195.10 meV
0 0	0 8	20.38	219.75 meV
0 1	0 10	18.41	173.93 meV
1 1	1 24	18.39	178.16 meV
0 1	0 21	15.56	219.97 meV
1 0	1 9	15.09	202.97 meV
1 0	1 1	12.87	100.85 meV

Table 3.2: Oscillator strengths,f, between states (L, K) and (L', K'), for the most probable optical transitions for the device shown in Fig. (3.11). The last column shows the energy of the transition.

An Auger process is not neglected in this system. There is the probability that by Coulombian scattering, other electrons in neighboring energy levels provide the extra energy to excite electrons in $(L = 1, K = 1)$, or otherwise, to continuum levels of the system. This electron is later collected by the contacts contributing to the photocurrent. It is in that sense that we call those bounded uppermost states as "mediator"-levels, for instance, $(L = 1, K = 24)$, $(L = 0, L = 21)$ and others, independently if they belong to the quantum dot or to the quantum well states [35].

We changed the height of the quantum dot to be 8 nm, in order to see the relative change in the energy levels. This allows us to fit in a better way the central energy of the experimental photocurrent peaks, as shown in table (3.3) for the first four energy levels of the system.

We note that the change in the energy levels is of the order of $\pm(10 - 20)\ meV$. The height of the quantum dots in our samples varies from $6 - 8\ nm$ and, there-

(L, K)	$h_0 = 7\ nm$	$h_0 = 8\ nm$	δE
0 0	93.50 meV	81.95 meV	11.55 meV
1 0	122.54 meV	110.52 meV	12.02 meV
0 1	154.69 meV	143.57 meV	11.12 meV
1 1	223.39 meV	206.27 meV	17.12 meV

Table 3.3: Difference, δE, in the energy levels calculated for a quantum dot with height of 7 nm and a quantum dot 8 nm high.

fore, a broadening of at least $(10 - 20)\ meV$ in the experimental curves is to be expected, oscillator strengths are not much affected by this change of dot height, however other transitions that were unlikely for 7 nm, appear in the case of the transition $(L = 1, K = 1) \rightarrow (L' = 1, K' = 22)$, with high probability, $f = 16.53$. This transition also supports our statement with respect to the "mediator"-levels since its density of probability in the rz-plane is similar to that for $(L = 1, K = 24)$ (see Fig. 3.14). The theoretical energy transition for the first peak is 95.75 meV and $f = 9.73$. Compared with the experimental PC spectra, there are two strong transitions with energy close to the central energy of the broad peak $\sim 225\ meV$. These are $(L = 0, K = 0) \rightarrow (L' = 0, K' = 8)$ with $f = 24.16$ and $E = 230.48\ meV$, and $(L = 0, K = 0) \rightarrow (L' = 0, K' = 7)$ with $f = 26.70$ and $E = 225.84\ meV$. We note, however, that the calculation of the transition energies as performed at zero *bias*, while the values quoted above are for 400 mV, 500 mV applied across the whole structure. These values correspond to an electric field $\sim 3\ kV/cm$, which should affect somewhat the energies of the transitions. It should be pointed out that even at zero applied *bias* there is an intrinsic electric field present in the structure due to transfer of charge from the contact layers to the quantum dots. Nevertheless, the agreement with the experimental result is good and allows one to have a better understanding of the physical processes involved in the generation of the transitions from the occupied electron levels have relatively deep final states, another process such as a two photon absorption or Auger scattering has to be involved in the photodetection.

All these results show that the method exposed in this chapter works! The results of its implementation for the characterization and designing of QDIP and QWIP devices is in good agreement with the experimental results. The introduction of other kinds of potential such as those cited in the previous sections and specially the consideration of the applied *bias* is possible, in order to get more realistic results. A parallelized version of this program was built to reduce the calculation times, and facilitate the study of more complex heterostructure.

Conclusions and Perspectives

Along this work, we present the study of the optical characteristics of two semiconductor heterostructures: micropillars and quantum dot infrared photodetectors. The first of these was studied with the code CAMFR, modelling the quantum dot system as a classical dipole, in order to understand the dependence of the excitation process of cavity modes in micropillars on the structural parameters of the quantum dots, such as their shape, position and orientation. We showed by a comparison of the theory here developed with the experimental results that the relative excitation intensity of the three lowest energy excited modes depends strongly on quantum dot orientation and polarization. We propose that the relative intensity of these excited modes can be used as an indirect method to determine the polarization of the quantum dot emission, including polarization along the growth direction, which presents a great experimental difficulty to be measured. These results and the conclusions from this work were published in Optics Express, Vol. 16, No 23, pag.19201, (2008).

The numerical implementation of the method proposed by Gangopadhyay and Nag [18], for the theoretical study of semiconductor heterostructures was sucessfully done. A C-code was built and a parallelized version developed in order to reduce the computational times, and allow the study of more complex structures that combine quantum dots, quantum wells and quantum wires, if any. As shown in the previous chapters the good agreement between the theoretical and experimental results, for a sample studied

in this work. Routines to compute optical features such as oscillator strength, density of probability mappings, and Auger scattering are included in the final code. The code can be compiled to be used in the Windows operative system, even though we recommended to run this in Linux for complex structures.

The work reported here can be used for the investigation of different structures, such as two dimensional photonic crystal, on which there is experimental working progress in our laboratory, and in the development and understanding of new innovated semiconductor heterostructure photodetectors.

APPENDIX

Appendix A

Numerical Codes Used

In this appendix, we present the complete CAMFR code used in order to make the studies of the pillar microcavity. An introduction to the mergement of the code developed for the photodetectors is made. The interested reader who wants to know more about this, please contact us: *cparra@fisica.ufmg.br*.

A.1 CAMFR: Cavity Modeling Framework

CAMFR is a Python script based in C++ programming language, which allows one to solve vectorially the Maxwell equations for any 1D, 2D and 3D structure with planar or cylindrical geometry. Thus, this free software can be used to study a big variety of photonic structures such as:

(i) Micro-structures in wavelength scale, e.g., photonic crystals, micropillars and other types of optical microcavities;

(ii) Lasers;

(iii) Light emitting diodes.

In chapter 2, we exposed the method in which this software is based. The following are some of the characteristics that it can be computed:

(i) Dispersion matrix of the structure.

(ii) Inward-propagating fields of the structure for a well defined excitation, either transverse or circular modes.

(iii) Characteristics of the laser modes: gain threshold and resonance wavelength of the material.

(iv) Source response in cavities.

The following is an example of the code used for the calculations:

```python
#/usr/bin/env python
####################################
# Construyendo la microcavidad
####################################

from camfr import *
set_N(100)
set_circ_order(1)


# Defining materials and parameters
GaAs_n = Material(3.5)
AlGaAs_n = Material(3.0)
air_n = Material(1.0)


# Defining geometric parameters
work_space = 10
d_GaAs = 0.0694
d_AlGaAs = 0.0809
r_core = 3
```

```
N_capas_der = 20

N_capas_izq = 20


# Defining PML conditions

set_circ_PML(-0.1)

# Defining source parameters and material gain

source_pos = Coord(0,0,cavity_pilar)

orientacion = Coord(1,0,0)

gain_n = Material(3.5)

set_gain_material(gain_n)


# Defining layers

capa_GaAs = Circ(GaAs_n(r_core)+air_n(work_space−r_core))

capa_AlGaAs = Circ(AlGaAs_n(r_core)+air_n(work_space−r_core))

space = Circ(air_n(work_space))


# Pillar top

top = Stack(2*capa_GaAs(d_GaAs)+N_capas_der*(capa_AlGaAs(d_AlGaAs)

+capa_GaAs(d_GaAs))+space(0))

# Pillar bottom

bottom = Stack(2*capa_GaAs(d_GaAs)+N_capas_izq*(capa_AlGaAs(d_AlGaAs)

+capa_GaAs(d_GaAs))+space(0))

# Setting up the cavity

cavidad = Cavity(top,bottom)

# Computing spectrum

outfile = file("Picos01/Pico-R"+str(r_core)+".dat",'w')

for l in arange(0.949,0.951,0.0001):
```

```
set_lambda(l)

cavidad.set_source(source_pos,orientacion)

potencia = top.ext_S_flux(0,r_core,)

print l,potencia

print >> outfile, l, potencia

outfile.close()
```

A.2 Numerical Calculations of Energies and Wavefunctions of Heterostructures

Now, we show how to use the code built to compute the energies and wavefunctions of any structure, even if this contains quantum dots. At the moment only two types of dot shapes are included in the program, cylinder dot shape and truncated cone dot shape. Specifically, the code was built in C-language and the GNU Scientific Library (GSL), and Message Passing Interface library (MPI) were also used.

The structure is defined in a param.txt data file, as follows

```
Pos   Material  Size(Ans)  x     y     type
---   --------  ---------  ----  ----  -------
0     InP        500.0     null  null  Barrier
1     InAs        20.0     null  null  Wetting
2     InAs        75.0     null  null  qdot
3     InP        500.0     null  null  Barrier
```

in which the structure is defined from bottom to top, with the coordinate system origin in the bottom. In this case, we have a InAs-quantum dot embedded in InP with wetting layer. The concentrations of the compounds for ternary and/or quaternary are also specified in the param.txt. The concentrations of these are put as x and/or y, depending of type of material. The "null" is written if this concentration is not included, for instance, a binary material does not need to specify the concentrations, and for a ternary material one just needs to specify x. The unit of length is Angstroms ($\AA$) and `type` refers to the function of the layer in the heterostructure. After this, in order to set the radius of the dot and the external cylinder, set the dimension of the basis, dot position in the structure, dot shape parameters and others, it is necessary to open the file called `GLOBAL_CONSTANTS.h`, in which all these parameters can be controlled, which are defined as global constants. Other kinds of potential, specially linear and parabolic, can be introduced by setting its position in the structure, initial and final potential, and their concentrations.

In order to compile the Linux version of the program, a Makefile was made, and the commands to compile and run it in a Linux console, are:

```
$ make clean
$ make
$ make run
```

The parallelized version is running in the same way, however, depending of the permission of the node (computer), i.e., if the cores have public access or not, the user will need to login in every core, after to execute the lines above.

At the moment, a version to run on the Windows operative system is being adapted.

The output files are saved into the file **Results**. The contents of these output files is to be understood as following:

- The energies are saved in data files called: `ENERG_L`l`.dat`, for $l = 0, 1, 2...$. It contains all energy values that the user asks for. In order to plot each one of these energies in a CB(VB) profile scheme, a similar data file is created in the process, `ENERG_L`l`_K`k`.dat`, which denotes the energy level (L, K).

- In a similar way, the eigenvectors that expand the wavefunctions of the system are saved as `VECTOR_L`l`_K`k`.dat`.

- The potential profile along the growth direction and the dot shape in the zr-plane are saved in the data files `Potential.dat` and `Qd_shape.dat`. The units of the potential for plotting are eV's and nanometers.

- The oscillator strengths are saved as `Osth.dat`. The wavefunctions are saved depending of the type of this, i.e., if the user needs the wavefunctions along the growth direction, these are saved as `WAVEFUNCz_L`l`_K`k`.dat`, and if the mappings are desired the data files are `WAVEFUNCPlanezr_L`l`_K`k`.dat`. The programm also generates the figure of these mappings in eps format.

- The routine for the Auger rates is about to be included in the program, and will be saved in the data files `AugerScatt.dat`.

It is possible to create new routines that make other kinds of processes and include them easily in the program. We expect that with this information the user can work with the program and obtain the desired results. This information is also included in a file README.txt in the final version of the program.

Bibliography

[1] Full-wave http://www.rsoftinc.com.

[2] Chalcraft A. R. A., Lam S., O'Brien D., Krauss T. F., Sahin M., Szymanski D., Sanvitto D., Oulton R., Skolnick M. S., Fox A. M., Whittaker D. M., Liu H. Y., and Hopkinson M. Mode structure of the l3 photonic crystal cavity. *Appl. Phys. Lett.*, 90:241117, (2007).

[3] N. W. Ashcroft and N. D. Mermin. *Solid State Physics*. Thomson Learning, Inc., (1976).

[4] V. N. Astratov, S. Yang, S. Lam, B. D. Jones, D. Sanvitto, D. M. Whittaker, A. M. Fox, M. S. Skolnick, A. Tahraoui, P. W. Fry, and M. Hopkinson. Whispering gallery resonances in semiconductor micropillars. *Appl. Phys. Lett.*, 91:071115, (2007).

[5] Pallab Bhattacharya, Xiaohua Su, G. Ariyawansa, and A. G. Perea. high-temperature tunneling quantum-dot intersublevel detectors for mid-infrared to terahertz frequencies. *Proceedings of IEEE*, 95(9):1828, (2007).

[6] P. Bienstman. Rigorous and efficient modelling of wavelength scale photonic components, Ghent University, Belgium, (2001).

[7] P. Bienstman and R. Baets. Optical modelling of photonic crystals and VCSELs using eigenmode expanson and perfectly matched layers. *Qpt. Quantum Electron.*, 33.

[8] Peter Bienstmann. Cavity modelling framework, http://camfr.sourceforge.net.

[9] L. Busal, A. Alemu, and A. Freundlich. Band alignments and quantum confinemente in (111) GaAsN/InAs strain-balanced nanostructures. *Nanotechnology*, 15:S245, (2004).

[10] Li Chun-Fei. Finesse-enhanced ring resonator coupled mach-zehnder interferometer all-optical switches. *Chinese Phys. Lett.*, 21:90–93, (2004).

[11] Andreza Germana da Silva. Propriedades ópticas e elétricas de pontos quânticos semicondutores de inas, Universidade Federal de Minas Gerais, Belo Horizonte, Brasil, (2008).

[12] A. Dararei, A. Tahraoui, D. Sanvitto, J. A. Timpson, P. W. Fry, M. Hopkinson, P. S. S. Guimar aes, H. Vinck, D. M. Whittaker, M. S. Skolnick, , and A. M. Fox. Control of polarized single quantum dot emission in high-quality-factor microcavity pillars. *Appl. Phys. Lett.*, 88:051113, (2006).

[13] Yablonovitch E. and T. J. Gmitter. Photonic band structure: The face-centered-cubic case. *Phys. Rev. Lett.*, 63(18):1950–1953, (1989).

[14] P. W. Fry et al. Inverted electron-hole alignment in inas-gaas self-assembled quantum dots. *Phys. Rev. Lett.*, 84:733, (2000).

[15] I. Favero, G. Cassabois, A. Jankovic, R. Ferreira, D. Darson, C. Voisin, C. Delalande, Ph. Roussignol, A. Badolato, P. M. Petroff, and J. M. Gérard. Giant optical anisotropy in a single inas quantum dot in a very dilute quantum-dot ensemble. *Appl. Phys. Lett.*, 86.

[16] Tan F.S., Klunder D.J.W., Kelderman H., Hoekstra H. J. W. M., and A. Driessen. High finesse vertically coupled waveguide-microring resonators based on Si_3N_4-

SiO$_2$ technology. *Proceedings of 2002 IEEE/LEOS Workshop on Fibre and Optical Passive Components*, pages 228–232, (2002).

[17] Silva A. G., Parra-Murillo C. A., Valentim P. T., Morais J. S., Plentz F., Guimaraes Paulo S., Vinck-Posada H., Rodriguez B. A., Skolnick M. S., Tahraoui A., and Hopkinson M. Quantum dot dipole orientation and excitation efficiency of micropillar modes. *Opt. Exp.*, 16:19201–19207, (2008).

[18] Samita Gangopadhyay and B R Nag. Energy levels in three-dimensional quantum-confinement structures. *Nanotechnology*, 8:14, (1997).

[19] J. M. Gérard, D. Barrier, J. Y. Marzin, R. Kuszelewicz, L. Manin, E. Costard, V. Thierry-Mieg, and T. Rivera. Quantum boxes as active probes for photonic microstructures: The pillar microcavity case. *App. Phys. Lett.*, 69:1110–1113, (1996).

[20] M. Grundmann, O. Stier, and D. Bimberg. Inas/gaas pyramidal quantum dots: Strain distribution, optical phonons and electronic structure. *Phys. Rev. B*, 52:11969, (1995).

[21] Pinkse P. W. H., Fischer T., Maunz P., and Rempe G. Trapping an atom with single photons. *Nature*, 404:365–368, (2000).

[22] M. Helm. *The basic physics of intersubband transitions. In: Intersubband Transition in Quantum Wells.* : Physics and Device Applications I. Semiconductors and Semimetals, vol. 62 ch. 1, ed. by H. C. Liu, F. Capasso (Academic), San Diego, (2000).

[23] Hood C. J., Lynn T. W., Doherty A. C., Parkins, A. S., and H. J Kimble. The atom-cavity microscope: Single atoms bound in orbit by single photons. *Science*, 287:1447–1453, (2000).

[24] P. Jayavel, H. Tanaka, T. Kita, O. Wada, H. Ebe, M. Sugawara, J. Tatebayashi, Y. Arakawa, Y. Nakata, and T. Akiyama. Control of optical polarization anisotropy in edge emitting luminescence of InAs/GaAs selfassembled quantum dots. *Appl. Phys. Lett.*, 84.

[25] John D. Joannopoulos, Robert D. Meade, and Joshua N. Winn. *Photonic Crystals: Molding the Flow of Light.* Princeton University Press, (2008).

[26] Steven G. Johnson. Mit photonic bands http://ab-initio.mit.edu/wiki/index.php.

[27] E. O. Kane. *The k.p method.* : Physics and Device Applications I. Semiconductors and Semimetals, vol. 1 ch. 3, ed by R.K. Willardson, A.C. Beer (Academic), New York, (1996).

[28] C. Kistner, T. Heindel, C. Schneider, A. Rahimi-Iman, S. Reitzenstein, S. Hofling, and A. Forchel. Demostration of strong coupling via electro-optical tuning in high-quality qd-micropillar systems. *Opt. Express*, 16:15006–15012, (2008).

[29] C. Kittel. *Introduction to Solid State Physics.* Thomson Learning, Inc., (1996).

[30] Claus F. Klingshirn. *Semiconductor Optics.* Third edition, Springer, Heidelberg, (2007).

[31] D. N. Krizhanovskii, A. Ebbens, A. I. Tartakovskii, F. Pulizzi, T. Wright, M. S. Skolnick, and M. Hopkinson. Individual neutral and charged $In_xGa_{1-x}As$-GaAs quantum dots with strong in-plane optical anisotropy. *Phys. Rev.*, 72.

[32] B. F. Levine. Quantum-well infrared photodetectors. *J. Appl. Phys.*, 74(8), (1993).

[33] Carlos A. Parra M. Propiedades ópticas de micropilares, Universidad de Antioquia, Medellãn, Colombia, (2007).

[34] Mohamed B. El Mashade1, M. Ashry, and A. Nasr. Theoretical analysis of quantum dot infrared photodetectors. *Semicond. Sci. Technol. .*, 18:891–900, (2003).

[35] Janet L. Pan. Intraband auger process and simple models of the ionization balance in semiconductors quantum-dot laser. *Phys. Rev. B*, page 11272, (1994)-II.

[36] Carlos Gabriel Pankiewicz. Localização de pontos quânticos semicondutores via nanolitografia por oxidação anódica, Universidade Federal de Minas Gerais, Belo Horizonte, Brasil, (2009).

[37] Seonung-Hwan Park and Shun-Lien Chuang. Comparison of zinc-blende and wurtzite GaN semiconductors with spontaneous polarization and piezoelectric field effects. *J. Appl. Phys.*, 87:353, (2000).

[38] Matthew Pelton, Jelena Vučković, Glenn Solomon, Axel Scherer, and Yoshihisa Yamamoto. Three dimensionally confined modes in micropost microcavities: Quality factors and purcell factors. *IEEE, Journal of Quantum Electronics*, 38(2):170, (2002).

[39] Craig Pryor. Eight-band calculations of strained InAs/GaAs quantum dots compared with one-, four-, and six-band approximations. *Phys. Rev. B*, 57:7190, (1997).

[40] E. M. Purcell. Spontaneous emission probabilities at radio frequencies. *Phys. Rev.*, 69:681, (1946).

[41] A. Rogalski, J. Antoszewski, and L. Faraone. Third-generation infrared photodetector arrays. *J. Appl. Phys.*, 105:091101, (2009).

[42] H. Schneider and H. C. Liu. *Quantum Well Infrared Photodetectors: Physics and Applications*. Springer, Heidelberg-New York, (2007).

[43] V. Troncale, K. F. Karlsson, D. Y. Oberli, M. Byszewski, A. Malko, E. Pelucchi, A. Rudra, and E. Kapon. Excited excitonic states observed in semiconductor quantum dots using polarization resolved optical spectroscopy. 101.

[44] K. J. Vahala. Optical microcavities. *Nature(London)*, 424:839–846, (2003).

[45] I. Vurgaftman and J. R. Meyer. Band parameters for III-V compound semiconductors and their alloys. *J. Appl. Phys.*, 89:5815, (2001).

[46] Jelena Vučković, Matthew Pelton, Axel Scherer, and Yoshihisa Yamamoto. Optimization of three-dimensional micropost microcavities for cavity quantum electrodynamics. *Phys. Rev. A*, 66:023808, (2002).

[47] S. Yamamoto, F. Tassone, and H. Cao. *Semiconductor Cavity Quantum Electrodynamics.* Springer Tracts in Modern Physics, Berlin, (2000).

[48] Pochi Yeh. *Optical Waves in Layered Media.* John Wiley and Sons, ICN., Publication, Santa Barbara, (2005).

[49] Peter Y. Yu and Manuel Cardona. *Fundamentals of Semiconductors: Physics and Materials Properties.* Springer, Heidelberg, (1996).